University of Bremen

Alfred Wegener Institute, Helmholtz Centre for Polar and Marine Research

Master's Thesis

Simulations of Marine Isotope Stage 3 climate using maximal and minimal Ice sheet scenario with AWI-ESM-2.1

Author:
Umesh Dubey

Matriculation Number:
3123750

First Supervisor:
Prof. Dr. Gerrit Lohmann

Second Supervisor:
Dr. Martin Werner

Tutor:
Dr. Paul Gierz

December, 2021

Declaration of copyright

Hereby I declare that my Masters Thesis was written without external support and that I did not use any other sources and auxiliary means than those quoted. All statements which are literally or analogously taken from other publications have been identified as quotations.

Declaration with regard to publishing theses

I agree that for research purposes third parties can look into my thesis stored in the University archive.

Bremen, December, 2021 **Umesh Dubey**

Abstract

Marine Isotope Stage 3 (MIS 3) is a critical transition period between the relatively colder MIS 4 and Last Glacial Maximum (LGM) climate. It is marked by more pronounced seasonality and reduced greenhouse gases (GHGs) than the pre-industrial (PI) period, as well as by the presence of the Laurentide ice sheet (LIS) and Cordilleran ice sheet (CIS). This project performs simulations under pre-industrial and two different MIS 3 regimes (57.5 ka and 45 ka BP, where ka BP represents thousand years before present) using maximal and minimal ice sheet scenario of each selected time slices of MIS 3 regimes with AWI-ESM-2.1 (Alfred Wegener Institute–Earth System Model), a state-of-the-art climate model with unstructured mesh and low resolution, to examine the sensitivity of the simulated Atlantic meridional overturning circulation (AMOC) to MIS 3 insolation, GHGs, topography (including properties of the ice sheet) and examine the characteristics of the simulated large-scale atmosphere and ocean circulation, precipitation, ocean hydrography, sea ice distribution, and internal variability of MIS 3-maximal relative to those of in MIS 3-minimal ice sheet scenario. In the simulations with MIS 3 (maximal and minimal ice sheet scenario), Earth orbital parameters and GHGs forcing conditions applied, the AWI-ESM-2.1 simulation shows a JJA (June–July–August) warming and DJF (December–January–February) cooling over the mid and high latitudes and more precipitation in Intertropical Convergence Zone (ITCZ) are observed compared with minimal conditions. The simulated 57.5 ka BP (45 ka BP)-maximal global mean value, near-surface air temperature is ~1.14 ^{0}C (~2.31 ^{0}C) and sea surface temperature is ~0.36 ^{0}C (~1.36 ^{0}C) cooler, and more precipitation by ~0.36 mm/month (~3.81 mm/month) than the 57.5 ka BP (45 ka BP)-minimal, respectively. The presence of the LIS and CIS lead to an additional regional cooling over the Northern Hemisphere. The AMOC is deeper and intensified in maximal than minimal scenario. There is a decrease in the volume of Antarctic Bottom Water (AABW) reaching the Atlantic. At the same time, there is an increase in ventilation of the Southern Ocean, associated with a significant expansion of Antarctic sea ice and concomitant intensified brine rejection, invigorating ocean convection. The global mean value, 57.5 ka BP (45 ka BP)-maximal sea ice concentration is ~1.6% (~3.1%) thicker than the 57.5 ka BP (45 ka BP)-minimal, respectively with an expansion of sea ice in the

Nordic Seas during boreal winter (March) and summer (September), causes more saline water over these regions due to brine rejection while forming sea ice. In conclusion, I find that the simulations capture spatially heterogeneous responses of MIS 3 climate.

Acknowledgements

During my studies at the University of Bremen, I have been greatly inspired by the work of the Professors and their openness to answer any questions. I developed my interest in this subject thanks to the unique teaching style of Prof. Dr. Gerrit Lohmann. I'm extremely grateful to him for giving me the opportunity to work on this exciting project, to begin with. I owe a debt of gratitude towards Dr. Paul Gierz who came up with the brilliant idea of this project. He has advised and supported me throughout this project and I enjoyed working with him a lot.

Thanks to the relaxed working atmosphere at Paleoclimate Dynamics section at AWI, I was able to approach anyone for my queries. I would like to extend my gratitude towards everyone working there and especially towards Dr. Evan Gowan for helping me with ice sheet reconstructions and to Dr. Martin Werner for all my queries. This work wouldn't have been possible if not for the tools such as AWI-ESM-2.1 model developed by AWI and CDO to manipulate and analysis of Climate datasets.

A part of life is about learning from one's experiences and moving ahead and I'm grateful to my friends for their support, my parents and my brother for always being there and motivating me throughout my life. Lastly, I would extend my gratitude to the Institute of Physics, the University of Bremen for giving me the opportunity to study here and I would like to thank all my lecturers and tutors for providing me with constructive feedback throughout this journey.

Contents

Chapter 1

Introduction

MIS 3, a period about 60 ka to 30 ka BP during the last glacial cycle, was characterised by millennial-scale abrupt climate transitions. These events are known as Dansgaard–Oeschger (D-O) events, can be revealed by the Greenland oxygen isotope ice core records (Dansgaard et al., 1993). A D-O event consists of an abrupt transition from a cold stadial climate state to a relatively warm interstadial climate state, followed by a gradual return to cold stadial conditions (Huber et al., 2006). Such sudden warming events in Greenland were likewise quite synchronized by sea surface temperature (SST) variations, recorded in marine sediment cores from the North Atlantic Ocean (Bond et al., 1997).

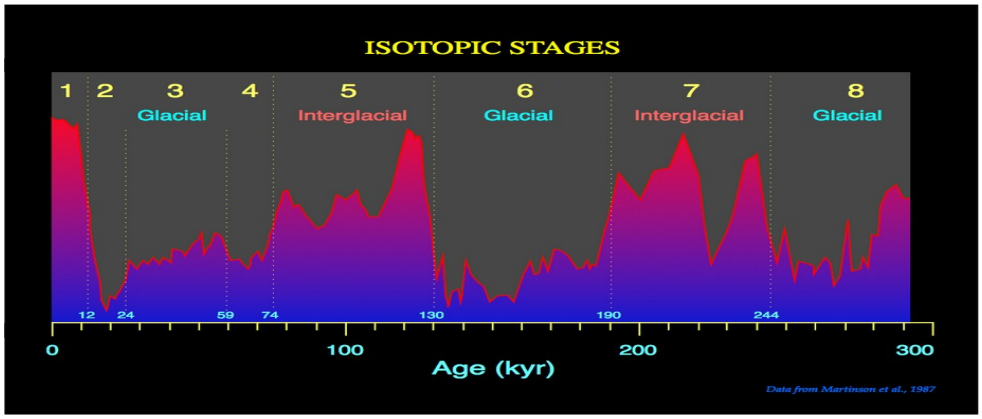

Figure 1.1. MIS 3 in stable oxygen isotope record of the last 300 ka years (Martinson et al.,1987).

These cycles are very well exposed by the relative content of ^{18}O isotopes ($\partial^{18}O$), or other proxy elements or substances contained in ice from polar ice cores, such as those in Greenland and Antarctica, as well as the variations of the same isotopes in marine sedimentary cores [for explanation of the $\partial^{18}O$ method, see Andrews, 2000]. In Fig. 1.1, the $\partial^{18}O$ variations during the last several glacial–interglacial cycles are depicted. The last glacial cycle, starting with the final phases of the last interglacial MIS 5, transitions into the intermediate MIS 4 and MIS 3 stages, followed by the LGM at MIS 2, and ends

in the Holocene (MIS 1). In this figure, isotope peaks pointing upwards correspond to warmer periods, whereas those pointing downwards are colder events.

Towards the end of every few stadial periods, the marine sediments show evidence of massive calving of the LIS, with large numbers of icebergs transversing and melting in the North Atlantic. These events are known as Heinrich events (Heinrich, 1988). The freshwater from these melting icebergs are thought to have weakened the salinity and hence Atlantic meridional overturning circulation (AMOC), possibly causing further cooling of the Northern Hemisphere (NH) (Broecker, 1994; Stocker, 1998).

The AMOC plays a crucial role in Earth's climate system. It has been shown that it may be affected by freshwater perturbations and changes in ocean temperature (Bryan, 1986; Clark et al., 2002; Manabe & Stouffer, 1995; Rahmstorf, 2002). Paleoclimate studies have found that its strength can be linked to abrupt climate changes in the past (Broecker et al., 1985; Keigwin et al., 1991; McManus et al., 2004). Examples for these changes are the so-called "Little Ice Age" (Bianchi & McCave, 1999; Broecker, 2000; Thibodeau et al., 2018) or the Last Termination and Heinrich Events (Barker et al., 2009, 2010; Broecker, 1990; Broecker et al., 1988; Knorr & Lohmann, 2007). With respect to global warming, several studies suggest a future slowdown (Gierz et al., 2015; Golledge et al., 2019; Stocker & Schmittner, 1997; Swingedouw & Braconnot, 2007; Weaver et al., 2012) and observations of sea surface temperature (SST), that can be used as a proxy for AMOC strength, already indicate a recent slowdown since the mid-twentieth century (Dima & Lohmann, 2010). However, the extent of the future weakening and the parts of different mechanisms affecting the AMOC are still unclear. One of these mechanisms is the potential future melting of the Greenland ice sheet (GIS), which might lead to the release of huge amounts of fresh water into the northern North Atlantic. Studies by Latif et al., (2000) and Lohmann (2003) suggest a strong atmospheric freshwater export from the Atlantic as an AMOC stabilizing effect in warm climates and those with a weak AMOC, respectively.

While there have been significant advances in our understanding of the dynamics behind D-O events in recent years, the key mechanisms triggering these abrupt climate transitions remain elusive. A leading hypothesis is related to a switch between strong, weak,

and off modes of the AMOC (Rahmstorf, 2002; Böhm et al., 2015; Henry et al., 2016). This has the potential to significantly alter the circulation and northward heat transport in the Atlantic Ocean. Model-based studies have shown that changes in the mode of the AMOC can be triggered by, e.g. freshwater input from melting ice sheets (Ganopolski and Rahmstorf, 2001) and variations in the size of the LIS (Zhang et al., 2014a), as well as changes in atmospheric CO_2 (Klockmann et al., 2018). Another theory for explaining the abrupt warming of Greenland invokes atmospheric circulation changes triggered by transitions in sea ice cover: e.g. Li et al., (2005, 2010) showed that shifts in Greenland precipitation and temperature are consistent with the climate response induced by sea ice growth and retreat, in particular over the Nordic Seas.

The sea ice acts as a lid, insulating the ocean from the atmosphere and reducing the amount of heat released. Proxy data from sediment cores in the Nordic Seas (Rasmussen and Thomsen, 2004; Dokken et al., 2013; Ezat et al., 2014) suggest that the warm Atlantic inflow can be separated from the sea surface by a halocline and slowly accumulate heat in the subsurface and intermediate/deep waters during MIS 3. Eventually, the warming below the halocline destabilises the water column and brings warm Atlantic water to the surface, tipping the Nordic Seas into an ice-free state that can lead to a rapid warming as seen in the Greenland ice cores (e.g. Dokken et al., 2013; Sadatzki et al., 2019).

Recent work in the Hudson Bay region in North America (Dalton et al., 2019) shows that during part of MIS 3, ice free conditions may have existed. Under this interpretation, the climatic conditions in this area were favourable to allow the growth of forests, with a climate that was potentially analogous to present. This would indicate that not only was the LIS reduced in size, it also had to be far enough removed from southern Hudson Bay to not strongly affect the climate there (Gowan et al., 2021).

MIS 3 is marked by pronounced seasonality and by the presence of the LIS. Even though recent data syntheses have improved the understanding of reconstructed data for paleoperiods and discrepancies between various records still make it difficult to obtain a comprehensive look at MIS 3 climate change (Brandefelt et al., 2011). Numerical climate model simulations can be used to improve our understanding of the mechanism behind MIS 3 climatic changes and to provide a coherent and physically consistent overview of the

climate on 100 to 1000 year time scales. The large ice sheet covering Fennoscandia during the LGM (21 ka BP) eroded most of the sequences that could have provided palaeoclimatological information for MIS 3 (Van Meerbeeck et al., 2009). The scarcity of regional palaeodata for MIS 3 and earlier periods lead to large uncertainties regarding the extent of earlier ice sheets and permafrost, and the length of ice free periods (Naslund et al., 2008). Here I use ESM models to investigate whether a realistic and consistent climate can be simulated during a specific MIS 3 time slice.

With the increasing concern over the possible extent of anthropogenically caused global warming, there has been a corresponding increase in demand for more rigorous climate model evaluation. While general circulation models of the Earth's climate are generally tuned and evaluated against present day conditions (Knutti et al., 2010), testing the ability of climate models to accurately reproduce the climate of the past extends this evaluation one step further, allowing for a more robust understanding of the models' skill in simulating any number of complex climate scenarios (Lohmann et al., 2013). Model intercomparisons of warm climates, both on longer time scales of several million years, such as the Pliocene (Haywood et al., 2013), as well as for more recent warm periods during the Quaternary, such as the Holocene (Bakker et al., 2014) or glacial period, such as MIS 3. (Bakker et al., 2013; Lunt et al., 2013), allow us to test how well a model can generally reproduce warm climates under external forcing and the resulting internal feedbacks. Model-data comparisons for various paleoclimates have generally been quite successful in past studies (Braconnot et al., 2012; Lohmann et al., 2013; Pfeiffer and Lohmann, 2016). However, since direct measurements of key climate variables such as temperature and precipitation are only available on a global scale for the last 130 years, paleoclimatology must rely on geochemical proxies to allow for the reconstruction of the climate state in the past; which necessitates the conversion of isotopic or chemical element ratios to climate variables like temperature or precipitation amount, a method subject to calibration and potential errors. More recently, paleoclimate modeling studies have begun to adopt a new method, enabling the climate models to directly simulate paleoclimate proxies.

In this thesis, I present MIS 3 (57.5 ka and 45 ka BP) simulations employing a new version of finite element climate model, AWI-ESM-2.1 (Alfred Wegener Institute– Earth

System Model), with unstructured CORE2 mesh and lateral resolution ranging from 20km to 160km, to simulate the MIS 3 climate (maximal ice sheet scenario) relative to the minimal ice sheet scenario and pre-industrial period (Appendix A) on a global scale. I will present typical climatic variables such as 2m air temperature (T_{2m}), 500 hpa geopotential height & wind speed, total precipitation (aprl + aprc), sea ice concentration (a_ice), sea surface temperature (SST) and respective AMOC response. This faster model throughput of approximately 90 model years per day can be achieved with existing hardware, compared to less 40 model years per day for the CMIP5 version of ESMs.

The simulations for 57.5 ka and 45 ka BP (maximal and minimal) scenario are configured with realistic boundary conditions presented in this thesis are integrated for ∼1500 model years each and the pre-industrial period is 1000 years. Trends in atmospheric temperature, oceanic temperature and salinity decrease towards the end of the simulation presented here and I therefore chose to use the term quasi-equilibrium to designate the simulated climate towards the end of my simulation (last 100 years of the model simulation). My experiments are forced by MIS 3 regimes involving the solar insolation and the GHGs forcings, and their combination with the presence of the LIS and albedo (0.7).

Given the small number of existing MIS 3 model studies, I aim to improve my understanding of MIS 3 climate, especially the baseline climate and the sensitivity of D-O-event-related variability to external forcing within a MIS 3 configuration. This master thesis is structured as follows: in Chapter 2, I give a brief overview of the AWI-ESM-2.1, including details of the version used in this study, followed by a description of the MIS 3 experimental configuration, ice sheets, topography & bathymetry, FESOM mesh resolutions, which are applied in the simulations, the CDO and the necessary statistical methods are described, and the motivation for selecting them is illustrated. Chapter 3 presents the results with respect to anomalous atmospheric and oceanic properties and sea ice in MIS 3 maximal with compared to the minimal ice sheet scenario. Chapter 4 provides discussions on the model resolution applied in the simulations, comparison of simulated MIS 3-maximal and MIS 3-minimal climates, simulated AMOC and model response to changes in GHG and ice sheet height are presented. The main conclusions are summarised in Chapter 5.

Chapter 2

Data and Methods

2.1 Model Description

The model is based on the AWI Earth System Model-2.1 (AWI-ESM-2.1) (Fig. 2.1), which consists of the AWI Climate Model-2-1 (AWI-CM-2-1) (Sidorenko et al., 2019), but with interactive vegetation and Northern Hemisphere ice sheet. The AWI-ESM-2.1 is a newly developed global coupled climate model which has been established at the AWI. The ocean and sea ice component is the Finite-Element Sea Ice–Ocean Model (FESOM-2.0; Danilov et al., 2017; Sidorenko et al., 2019), which is discretized on a triangular grid with a continuous conforming representation of model variables, whereas the atmospheric module is represented by the general circulation model ECHAM-6.3.05p2 (Stevens et al., 2013), mainly developed by the Max Planck Institute for Meteorology (MPI-M).

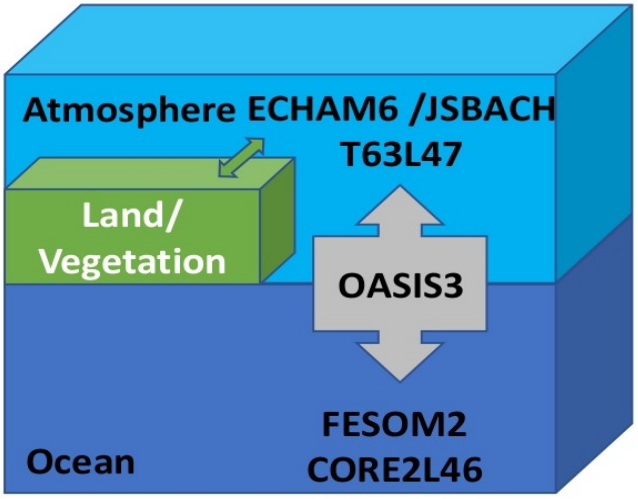

Figure 2.1. Schematic of the AWI-ESM-2.1 modelling toolbox with T63L47 setup. (https://fesom.de/models/awi-esm/)

ECHAM-6.3.05p2 is the sixth generation of the atmospheric general circulation model ECHAM, it focuses on coupling between diabatic processes, which are often associated with small-scale fluid dynamics and large-scale circulations. The model stems from an earlier release of the European Centre (EC) for Medium-Range Weather Forecasts (ECMWF) model (Roeckner et al., 1989). Like most models, the dynamics of ECHAM-6.3.05p2 is based on hydrostatic primitive equations (HPEs) with traditional approximation.

A Gaussian grid is used in the model to calculate non-linear equation terms and some physical representations. The boundary layer and turbulence parameterization are based on the eddy-diffusivity and viscosity approach. Momentum transport arising from boundary effects is parameterized using the subgrid orography scheme as described by Lott, (1999). Subgrid-scale cloudiness is represented using the assumed humidity distribution function scheme developed by Sundqvist et al., 1989. Radiative transfer in ECHAM-6.3.05p2 is represented using the rapid radiation transfer. ECHAM-6.3.05p2 also includes a land surface model (JSBACH-3.20) based on a tiling of the land surface and includes dynamic vegetation with 12 plant functional types and 2 types of bare surface.

FESOM-2.0 is a hydrostatic ocean circulation model based on the finite-element approach and designed to work on unstructured meshes; it is therefore different in many important respects from models formulated on regular meshes. For example, an advantage of FESOM-2.0 is its multi-resolution capability, which allows for regional focus in an otherwise global setup. The flexibility of the unstructured meshes allow to avoid the effect of geographic coordinates, so the meshes can be designed according to the distances along the spherical surface (Wang et al., 2014). Unstructured meshes enable narrow straits to be represented as through flows (Wekerle, 2013). The mesh nodes are vertically aligned to avoid difficulties in resolving the hydrostatic balance. The model uses variable resolution, which can be as fine as 20 km in the Arctic and along coastlines. A no-slip boundary condition along the coast is implemented in the model. Surface stress and buoyancy fluxes are derived from the ice– ocean coupling.

Internal coupling between ECHAM-6.3.05p2/JSBACH-3.20 and FESOM-2.0 is performed via the OASIS3-mct coupler. This model setup builds upon the work by Sidorenko et al., 2019, who present the coupled model setup ECHAM-6.3.04/JSBACH-3.11/FESOM-2.0, albeit without dynamic vegetation. My setup uses a newer version of both ECHAM-6 and JSBACH-3, which we upgrade to ECHAM-6.3.05p2 and JSBACH-3.20.

2.2 Experimental Design

In the following, I describe the experimental setup of the MIS 3 (maximal and minimal ice sheet scenario) and PI simulations. A summary of the experiment characteristics are provided in Table 1.

Table 1: Forcing and boundary conditions for both, maximal and minimal ice sheet scenario for the MIS 3 and PI simulations.

Experiments	**57.5 ka BP**	**45 ka BP**	**Pre-Industrial (PI)**
Orbital Parameters (kept same for both, maximal and minimal scenario)			
Eccentricity	0.0170	0.0129	0.0167
Obliquity	23.890^0	24.412^0	23.459^0
Perihelion – 180^0	248.94^0	250.94^0	102.72^0
Greenhouse Gases (kept same for both, maximal and minimal scenario)			
Carbon dioxide	217 ppm	204 ppm	284 ppm
Methane	540 ppb	410 ppb	808 ppb
Nitrous oxide	245 ppb	238 ppb	273 ppb
Other characteristics (maximal and minimal scenario)			
Solar constant	1360.9 W m^{-2}	1360.9 W m^{-2}	1360.9 W m^{-2}
Topography and maximal ice sheet scenario	57.5 ka BP (maximal)	45 ka BP (maximal)	Modern
Topography and minimal ice sheet scenario	57.5 ka BP (minimal)	45 ka BP (minimal)	Modern
Integration time	1500 years (each maximal & minimal)	1500 years (each maximal & minimal)	1000 years

Under the forcings: Orbital parameters and greenhouse gases are kept same for each MIS 3 (maximal and minimal) scenario simulations, but the boundary conditions: Topography and ice sheets size are different, and the integrations time (1500 years) are same in all four MIS 3 simulations. These simulations are chosen because it simply tests the response of the climate system to changes in orbital forcing compared to the present (Otto-Bliesner et al., 2017). The difference in the latitudinal and seasonal distribution of incoming solar radiation (insolation), which results from changes in the Earth's orbit, plays the central role for changes in climate during MIS 3 (Berger (1978). Studies on deep-sea sediment cores reveal that temperature peaks in paleoclimate are statistically correlated with the main periodicities in the Earth's orbital parameters, and show that orbital parameters are the main forcing in determining glacials and interglacials (Hays et al., 1976). Milutin Milankovic described in the 1940's that differences in eccentricity, axial tilt, and precession can significantly change climate patterns by changing the amount of incoming solar radiation (Milankovic et al., 1995; Fig. 2.6).

Using the circulation model AWI-ESM-2.1 at a low oceanic resolution as described in section 2.3, I perform total of five simulations: Four different MIS 3 runs (57.5 ka and 45 ka BP) of maximal and minimal ice sheet scenario plus a pre-industrial (PI) scenario, where MIS 3 minimal scenario and PI (Appendix A) are used as a reference, all by prescribing the appropriate forcings and boundary conditions (Table 1). Orbital parameters are calculated according to Berger (1978). In the PI experiment, the GHGs are prescribed according to the Paleoclimate Modeling Inter comparison Project (PMIP; Crucifix et al., 2005). In MIS 3 simulations, the GHGs are taken from ice-core records and from recent measurements of firn air and atmospheric samples (Köhler et al., 2017). The model uses adjusted ice sheet properties; for instance, the surface albedo is set to 0.7, and the amount of vegetation to zero.

2.3 FESOM Mesh Resolution

The atmosphere model ECHAM6, which is run with version “Echam-6.3.05p2” and the T63L47 setup, that is a horizontal resolution of $1.9^0 \times 1.9^0$. The ocean-sea ice model FESOM-2.0 employs an unstructured grid, allowing for varying resolutions from 20 km around Greenland and in the North Atlantic to around 150 km in maximal scenario whereas in minimal scenario it is from 20 km above North Atlantic to 150 km in the North Atlantic in the open ocean (CORE2 mesh). With the unstructured mesh, high spatial resolution can be applied in dynamically active regions while a relatively coarse resolution can be used elsewhere to reduce computational demands. The resolution ranges spatially from 20 km to 180 km, and 47 vertical z-level grids.

In FESOM-2.0, we increase the resolution across the entire North Atlantic, the coastlines, the equator, and the Southern Ocean, ensuring good representation of several key oceanographic processes — including deep and bottom water formation, equatorial dynamics, as well as coastal boundary currents. Fig. 2.2 shows the land - sea masks and CORE2 mesh resolutions used for my MIS 3 simulations. These resolutions are referred to as "low resolution", and abbreviated as LR, thus yielding the complete model name AWI-ESM-2-1-LR.

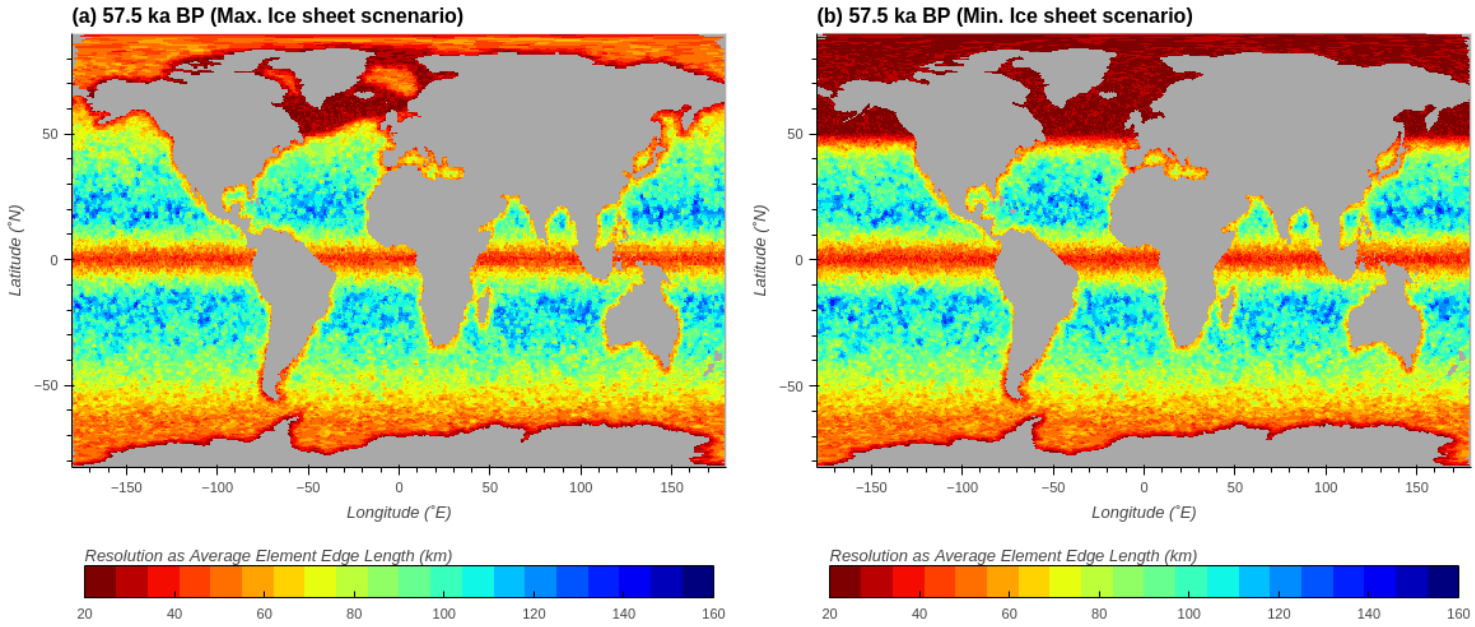

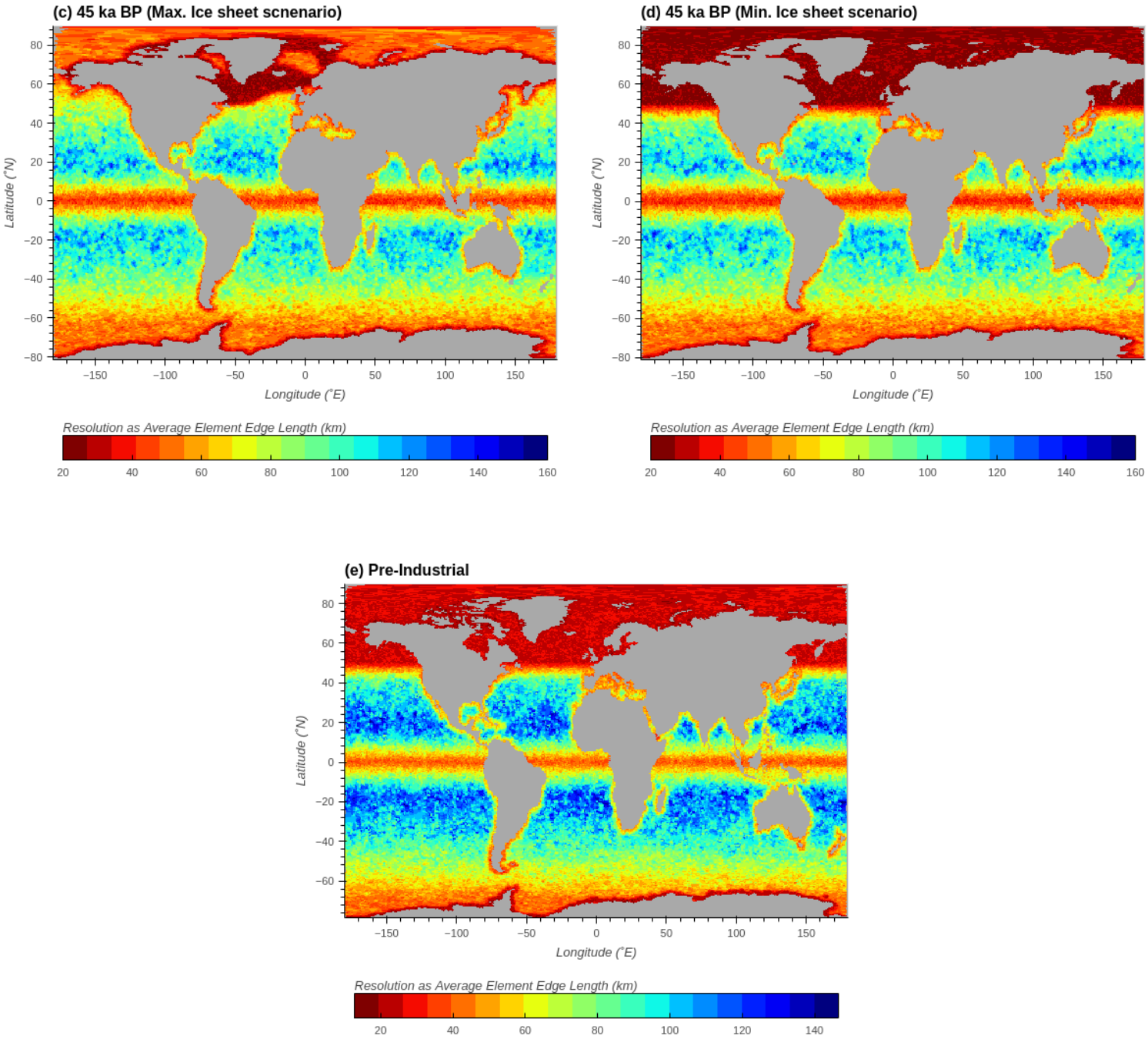

Figure 2.2. Land - sea masks (grey shading) and FESOM mesh resolution applied in MIS 3 simulations: (a, c) 57.5 ka and 45 ka BP of maximal ice sheet scenario, (b, d) 57.5 ka and 45 ka BP of minimal ice sheet scenario and (e) PI simulations, where mesh resolution defined as the average edge length of one triangular surface element. Units are Km.

2.4 Ice sheets, Topography, and Bathymetry

The configuration of global ice sheet extent and elevation (Fig. 2.3) is derived from a data-constrained ice sheet model for 57.5 ka and 45 ka BP consisting of the Antarctic, Greenland, North American, and Eurasian Ice Sheets. In this thesis the reconstructions of ice sheet of MIS 3 are based on Gowan et al., 2021.

The ice sheet reconstruction was calculated using modern topography using a shear stress model with values based on surface topography and surficial geology. The method was originally established by Reeh (1982) and Fisher et al., (1985). The ice sheet reconstruction, called PaleoMIST 1.0 (Paleo Margins, Ice Sheets and Topography), is constructed independently of far-field sea level and $\delta^{18}O$ proxy records are often used to constrain ice volume, which is based on Glacial isostatic adjustment (GIA) Method. GIA plays a role in determining the discrepancy between ice thickness and elevation changes. GIA based ice sheet reconstructions are commonly used for paleoclimate modeling and assessing present day Earth deformation and sea-level change. As a result, it is fundamental that the displayed history of the ice sheets follow to nearby topographical and geophysical imperatives as much as possible.

The North American MIS 3 margin extent is generally larger than the recent assessment by Batchelor et al., 2019, which was based on an older reconstruction. The validity of the chronological constraints that indicate a reduced ice sheet configuration in North America has been strongly criticized, so I present maximal and minimal reconstructions for MIS 3. The minimal reconstruction has a complete retreat of the ice sheet from Hudson Bay for a short period of time in MIS 3, while the maximal reconstruction maintains ice cover through all of MIS 3 (Gowan et al., 2021).

The altitude of the land surface is kept at pre-industrial values outside the ice sheet areas. In the areas covered by land ice, the maximum value of the original pre-industrial topography and MIS 3 reconstructed ice sheet topography is used; this procedure prevents jumps to high topography adjacent to the ice sheet margin. The resulting MIS 3 LIS (CIS) reaches altitudes up to 3600 m (3200 m) respectively, but is significantly smaller, both in terms of ice extent and height, when compared to the LGM ice sheets (Peltier et al., 2015).

Similarly, the Eurasian Ice Sheet is smaller, but there is a significant amount of ice sheet over Fennoscandia. The LIS is separated with the CIS in my MIS 3 ice sheet configuration. However, the shape of the MIS 3 ice sheet is highly uncertain; studies have also shown separated LIS and CIS before the LGM (Abe-Ouchi et al., 2007). Unfortunately, there is a lack of reliable geological evidence for the existence of land ice in the Barents Sea. However, sparse evidence from the Barents Sea–Svalbard region suggest there was little or no land ice here during MIS 3 (Ingólfsson and Landvik, 2013). Therefore, the Barents Sea is kept free of land ice with a reduced water depth in the MIS 3 configuration of the model. The Canadian Archipelago is covered by land ice, blocking the passage of water between Baffin Bay and the Arctic. In Antarctica (Fig. 2.4), the Ross and Weddell Sea are covered by grounded ice rather than floating ice shelves as today.

The ocean bathymetry is adapted based on an estimated sea level in 57.5 ka BP maximal (minimal) ice sheet scenario ~59 m (58 m) lower, and in 45 ka BP maximal (minimal) scenario sea level ~41 m (36 m) lower, respectively (Fig. 4.2) (Gowan et al., 2021). As a consequence, many shallow ocean grid points on the shelf turn into land, thereby modifying the land–sea mask (Fig. 2.3). Most of the modifications occur in the northern high latitudes, e.g. the East Siberian Shelf, Laptev Shelf, and the Bering Strait (which is closed). With the adjusted MIS 3 land–sea mask and surface topography, a new river-routing map is produced. For the ice-free land surfaces, the river routing corresponds to the PI simulation. Where there is new land, due to the lower MIS 3 sea level, the river outlets are extended to the ocean. For the ice covered areas, a new map is generated based on the land ice topography, routing the water from the land ice along the steepest gradient, either directly to the ocean or to the nearest river if the ice margin terminates on land.

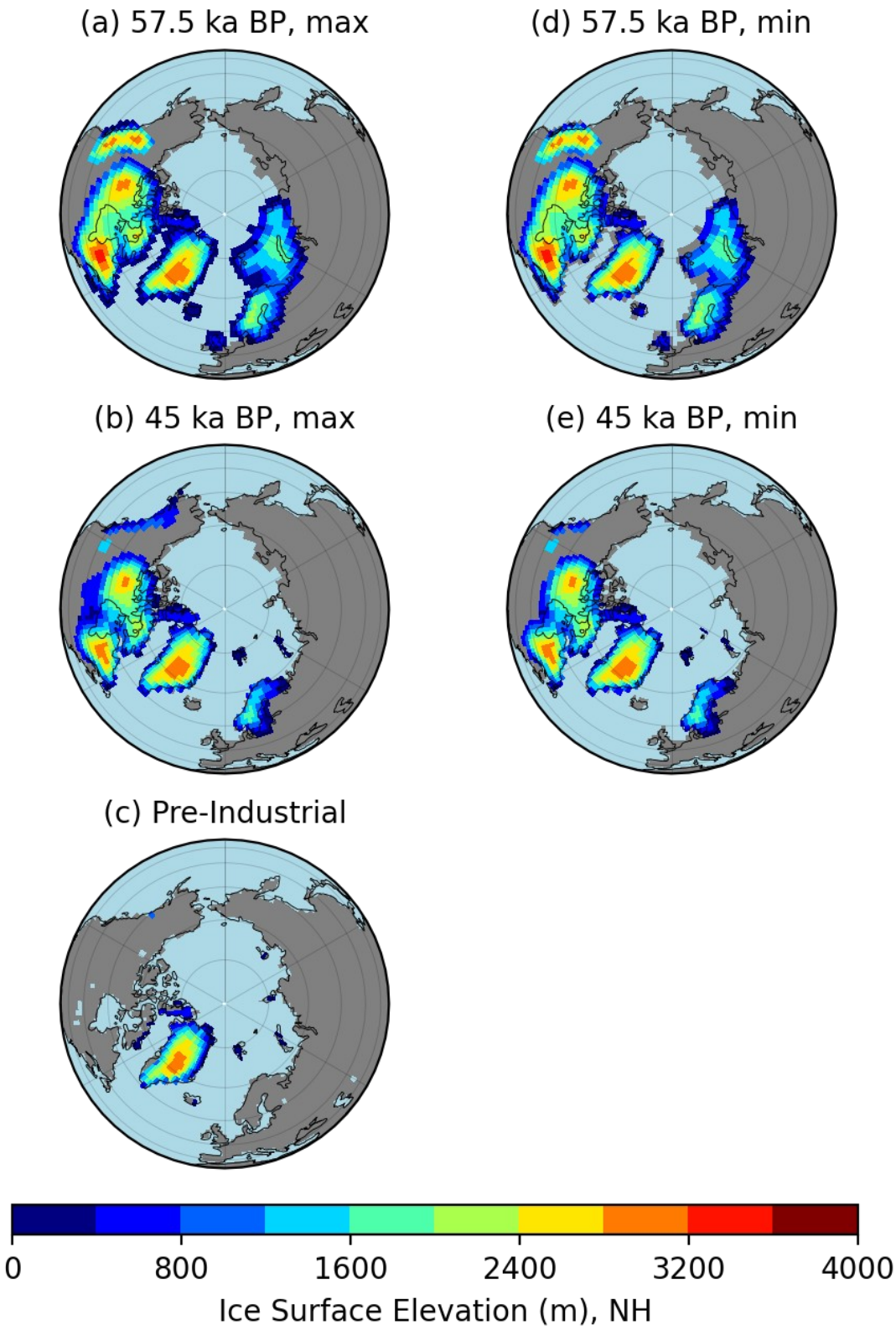

Figure 2.3. Land - sea masks (grey shading) and Ice surface elevation of MIS 3 for maximal (a, b), minimal (d, e) scenario and PI (c) in Northern Hemisphere (NH). Units are m.

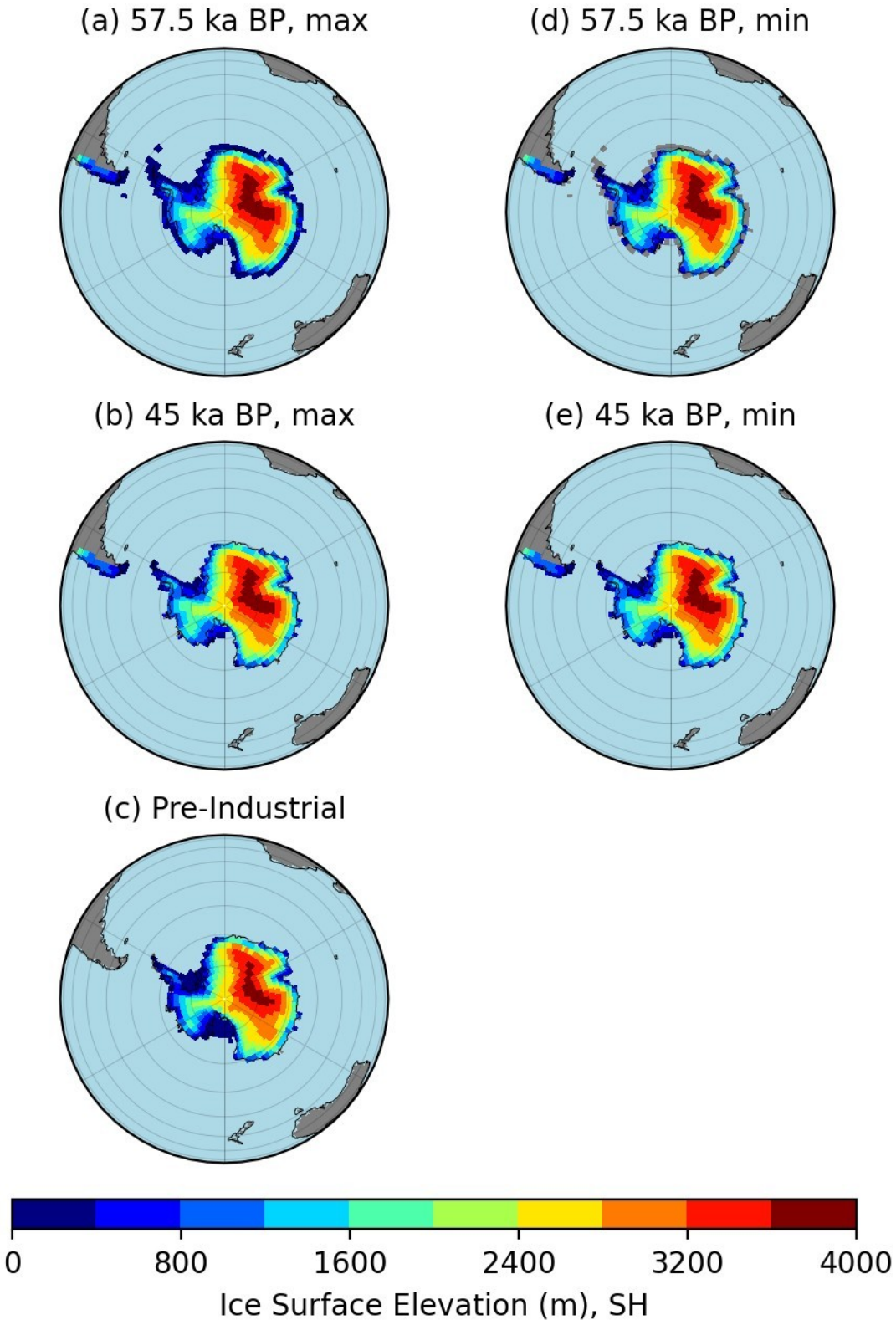

Figure 2.4. Land - sea masks (grey shading) and Ice surface elevation of MIS 3 for maximal (a, b), minimal (d, e) scenario and PI (c) of Southern Hemisphere (SH). Units are m.

2.5 Calendar Correction

It is important to note that the seasons defined based on classical calendar do not match up with the astronomical seasons with 90^0 segments of the orbit (Timm et al., 2008), hence a calendar correction will be applied for the purpose of the experiment.

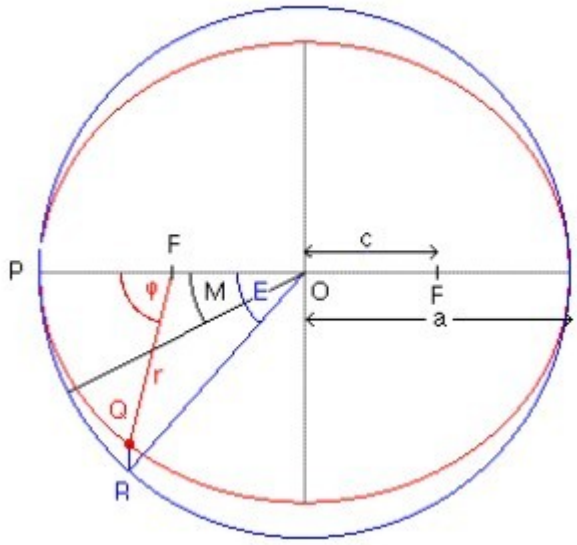

Figure 2.5. The mean, eccentric and true anomaly. Here stands for the true anomaly, defined as the angle between the perihelion on the major axis of the orbit ellipsoid and the current position of Earth; M the mean anomaly, i.e. the angle between the perihelion and Earth's position based on the assumption that the orbit would be a perfect circle; and E the eccentric anomaly, which is an angular parameter that defines the position of a body that is moving along an elliptic Kepler orbit. F is the position of the Sun and Q the position of the Earth. P represents the position of perihelion.

When prior annual cycles are compared to today's fixed calendar, significant biases can emerge. Observing how the Earth's orbital parameter varies over time. The slow decrease in eccentricity from almost 0 to 0.0607 can be attributed to the induced change in the amount of annual mean total insolation received by the Earth. Obliquity oscillates from 22^0 to 25^0 and the position of the equinoxes precesses relative to the perihelion all over some period of time. However, it is important to take these changes into consideration hence there is a need to define a reasonable calendar for the past. When defining seasons contained in a 12-month

calendar with its respective configuration, it is important to compare seasonal climate to the Earth’s position along its orbit.

The real anomaly of the Earth is defined as the angle between the perihelion on the major axis of the orbit ellipse and the Earth's current position, while a month is defined as a 30^{0} increment of the true longitude as seen from a stationary place. As previously noted, this fixed location is normally the Northern Hemisphere vernal equinox, which occurs on March 21st, equivalent to 81 in the calendar year. The Calendar conversion mainly consists of; Defining angular calendar and computing unbiased monthly means directly using daily model output and/or converting old monthly means into new monthly means if there is no daily output available.

2.6 Radiative Forcings

The amount of insolation in NH mid and high latitudes are mostly controlled by the obliquity (the tilt of the Earth's axis of rotation) and precession (the precession of the Earth's axis of rotation) signals. A major difference in the forcing during MIS 3 as compared to the PI is the seasonal and latitudinal distribution of the incoming solar radiation (Fig. 2.7). The largest absolute differences between MIS 3 and the PI are found in the high latitudes. The latitudinal gradient in MIS 3 minus PI insolation difference is due to the combined effect of obliquity and precession differences. Obliquity was higher during MIS 3, with large differences between winter and summer insolation as a result. Precession influences the direction of the Earth's axis of rotation with respect to the Sun such that the NH (SH) has a stronger seasonal cycle in insolation for MIS 3 (PI).

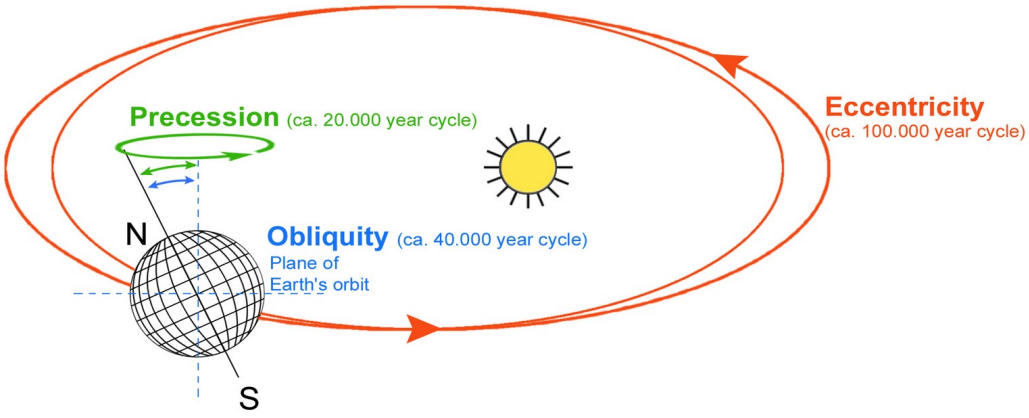

Figure 2.6. The Earth's three main orbital variations (Milankovich cycles) that drive the ice age cycle. **Eccentricity**: changes in the shape of the Earth's orbit. **Obliquity:** changes in the tilt of the Earth's rotational axis. **Precession:** wobbles in the Earth's rotational axis. (https://paleodyn.uni-bremen.de/study/MiloGesamtKopie.jpg)

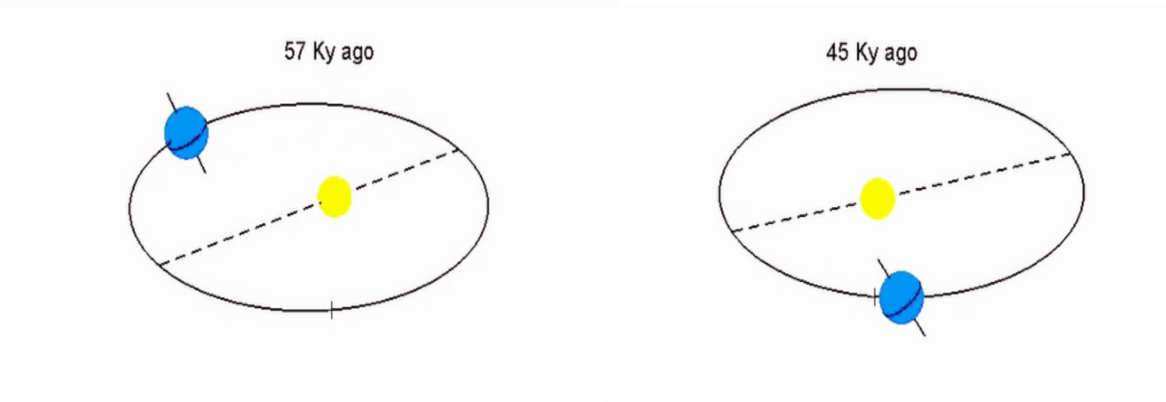

Figure 2.7. The Earth's position relative to the Sun during MIS 3.
(https://paleodyn.uni-bremen.de/study/Orbit.m4v)

The orbital forcing used in the model was calculated following Berger (1978). Compared with the modern situation, the annual cycle at mid and high latitudes was amplified at MIS 3, most notably with more insolation during summer and less in winter. The solar constant is kept fixed at MIS 3 (maximal and minimal scenario) and PI values (1360.9 Wm^{-2}), and the orbital parameters are set to values corresponding to 57.5 ka and 45 ka BP. In the NH, the chosen MIS 3 time slices, 57.5 ka shows enhanced insolation in summer (June-July-August) and 45 ka shows enhanced in (May-June-July) relative to present (PI), followed by reduced summer insolation (July-August-September) of MIS 3. In the SH, changes in insolation are more pronounced in 57.5 ka and less at 45 ka BP, with stronger fall of insolation (October-November-December) for 57.5 ka, (September-October-November-December) insolation for 45 ka BP and weaker winter insolation (January-February-March) and (February-March) for 57.5 ka and 45 ka BP, respectively relative to PI (Fig. 2.8, a, b, c, d). The boreal summer at 57.5 ka and 45 ka BP are both at aphelion, while obliquity is the lowest and highest respectively. Lower obliquity reduces the insolation received over polar regions during both hemispheric summers, while there are increases in the insolation received during winter especially for the Southern Hemisphere (Fig. 2.8, e, f).

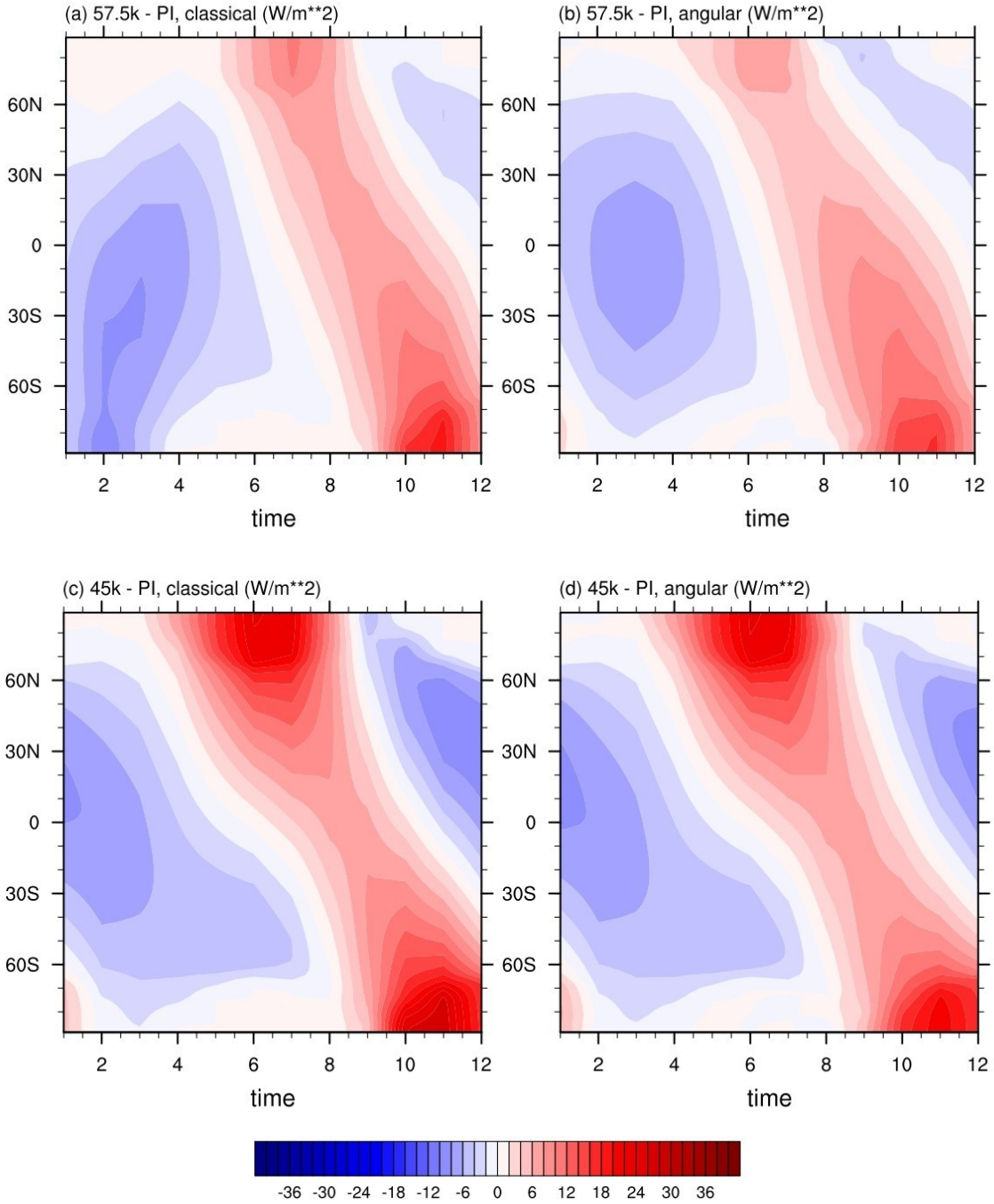
(a) 57.5k - PI, classical (W/m**2)
(b) 57.5k - PI, angular (W/m**2)
(c) 45k - PI, classical (W/m**2)
(d) 45k - PI, angular (W/m**2)
60N
30N
0
30S
60S
2
4
6
8
10
12
time
-36 -30 -24 -18 -12 -6 0 6 12 18 24 30 36

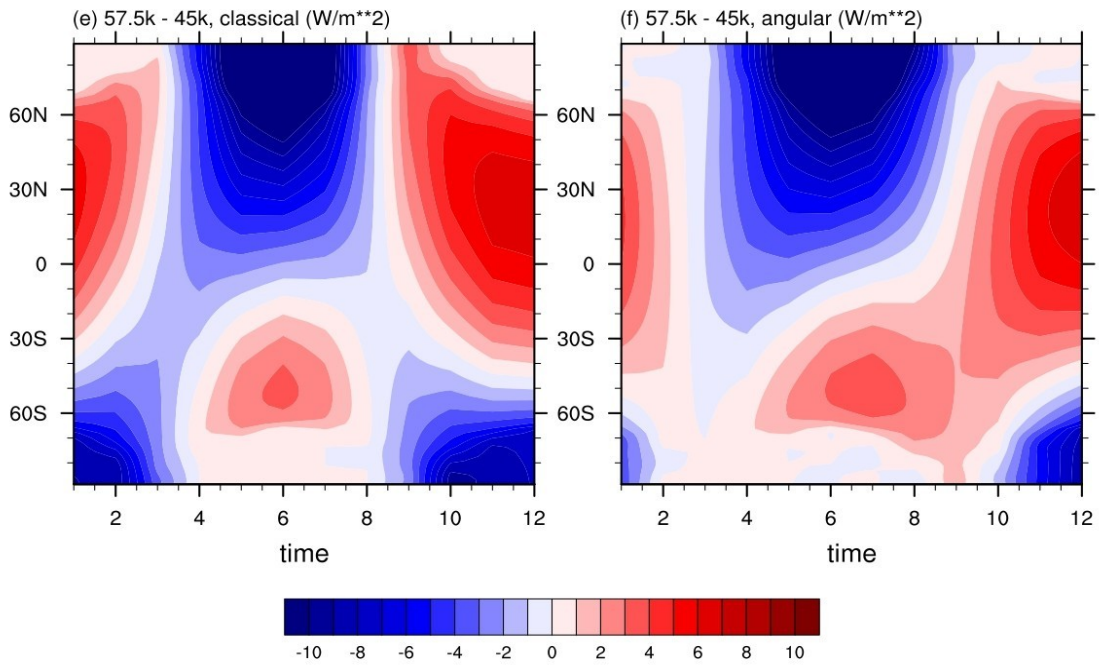

Figure 2.8. Latitudinal insolation anomalies of MIS 3 relative to PI and 57.5 ka relative to 45 ka BP for (a, c, e) classical calendar and (b, d, f) angular calendar. Where time is considered as month and insolation units are W m^{-2}.

2.7 The Climate Data Operator (CDO)

CDO is a command line suite for manipulating and analysing climate data. It provides more than 700 operators which can process climate and forecast model data. The operators perform simple statistical and mathematical functions, data selection and subsampling, and spatial interpolation. CDO was developed to have the same set of processing functions for GRIB (General Regularly-distributed Information in Binary form) and NetCDF (Network Common Data Form) datasets in one package (Schulzweida et al., 2006).

The following are the primary CDO features that were used to conduct this thesis:

- UNIX command-line interface that is simple to use. A dataset can be processed in a realistic manner by serially executing numerous consecutive operators without

saving the interim results in files, which is critical for processing the vast volume of daily model output.

- fast processing of large datasets.
- dedicated operators for computing the variables annual and seasonal means.
- It supports the ECHAM T63 grid and, with the help of the code table provided by ECHAM6, the meaning of any output variable is well understood.

2.8 T-Test Analysis for Comparing Climate Anomalies

The statistical significance of the calculated trends is tested using the Student's t test with the number of degrees of freedom, accounting for autocorrelation, calculated following Bretherton et al., 1999.

The t-test is one of the more basic statistical procedures for hypothesis testing. There are various types of t-tests. The two-sample t-test, commonly known as the Student's t-test or the independent samples t-test, is the most frequent and is used to analyze mean value data sets to identify inconsequential anomalies. The independent samples t-test determines if the means of two sets of data differ significantly when the data come from two different groups of participants under different circumstances (O'Mahony, 1986). Trends with p values < 0.05 are considered to be statistically significant.

A t-test can be calculated by using the following formula:

$$t = \frac{difference\ between\ means}{standard\ error\ of\ difference} = \frac{\bar{x}_1 - \bar{x}_2}{\sqrt{\frac{S_1^2}{N_1^2} + \frac{S_2^2}{N_2^2}}}$$

where, $\bar{x}_1$ and $\bar{x}_2$ are the means for the two independent samples (difference between means), and S_i^2 is the unbiased estimator of the variance of each of the two samples with N_i

being the number of samples in group i. t will be large, if $\bar{x}_1$ and $\bar{x}_2$ is large compared to the standard error of the difference. The standard error term can be identified as a measure of the potential random variation, or experimental error, in the experiment. As a result, if the differences between the two samples are significant as compared to experimental deviation or noise, they are significantly different (t is large; O'Mahony, 1986).

In the results, the two-sample t-test is used to identify insignificant difference in the surface air temperature, precipitation and sea surface temperature anomalies of the simulated MIS 3 maximal relative to the minimal ice sheet scenario and PI climate, respectively (Appendix A), and the marked area has a significance level of above 95% based on Student's t-test.

Chapter 3

Results

The MIS 3 experiment, 57.5 ka and 45 ka BP, both maximal and minimal ice sheet scenario were run for 1500 years each and 1000 years for the PI experiment. In terms of my statistical analysis for the time slice experiments, I only take into account the integration periods (last 100 years of the model simulation) after the spin-up with trends in global SST not exceeding 0.05°C per century a stable AMOC, according to Braconnot et al., 2007. Once runs were initiated for the time slice experiment, no changes to the forcing were permitted. Consequently, all of the simulated climatic fluctuations are generated by internal climate variability in the coupled system. The seasonal (winter - DJF and summer - JJA) and annual mean climatology are calculated using CDO by averaging the corresponding parameters over the entire valid integration periods. In the following results, I explore the climate responses to different MIS 3 forcings (maximal ice sheet scenario) relative to minimal ice sheet scenario and PI (Appendix A).

Table 3.1: Global mean values for the MIS 3 (maximal and minimal ice sheet scenario) and PI experiments.

Simulation	**T_{2m} (^{0}C) ≈**	**Precipitation (mm/month) ≈**	**Sea ice concentration (%) ≈**	**SST (^{0}C) ≈**
57.5 ka-maximal	9.49	66.88	60.5	15.12
57.5 ka-minimal	10.63	67.24	58.9	15.48
45 ka-maximal	8.39	65.19	62.2	14.23
45 ka-minimal	10.70	69.007	59.1	15.59
PI	12.59	71.88	50.6	16.49

3.1 Atmospheric Surface Temperature

The simulated 2m surface temperature (T_{2m}) anomalies of 57.5 ka and 45 ka BP maximal compared with minimal ice sheet scenario are depicted in Fig. 3.1. In both hemispheres, significant cooling occurs at low and high latitudes. This is especially evident above the LIS and Scandinavian Ice Sheet, which is thicker and larger in the maximal than minimal scenario of MIS 3, and where cooling reaches up to 10 ^{0}C in 57.5 ka and up to 8 ^{0}C in 45 ka BP, as well as in the Barents Sea and parts of the Nordic Seas, where sea ice expands. The 2m surface temperature over land respond faster than the ocean due to lower heat capacity. In other words, the continents are in general cooler in winter, and warmer in summer over high latitudes for 57.5 maximal than minimal scenario. However, consistent warming is shown in higher latitudes of the ocean (specially over the North Pacific & North Atlantic) and on land (over the Alaska & northern part of Canada, northern Europe in boreal summer) up to 6 ^{0}C warming in 57.5 ka (maximal - minimal) simulations, all year round. This is probably due to the larger heat capacity of the ocean and the residual effect of sea ice that lasts from previous summer and also the reasons are the ice sheet volume difference in between maximal and minimal scenario is lower in 57.5 ka than in between the 45 ka BP maximal and minimal scenario (Fig. 2.3). Whereas on the other hand cooling can be seen globally in 45 ka BP (maximal – minimal) except the warming over the Southern part of North America.

Simulated annual and seasonal mean T_{2m} changes (MIS 3 - PI) are shown in Fig. A.1, A.2. The dominant cooling of annual mean temperature values results from the combined effect of the insolation changes and reduced GHGs and more pronounced coolings are found up to 13 ^{0}C in 45 ka and up to 15 ^{0}C in 57.5 ka BP at the higher latitudes regions (specially over LIS and Scandinavian Ice Sheet) in NH. This is particularly clear above the LIS and CIS, as well as in the Barents Sea and parts of the Nordic Seas, where sea ice expands (Fig. 3.4, 3.6). A significant boreal winter cooling of up to 14 ^{0}C compared with PI conditions, forced by the negative DJF insolation anomalies, is found over the NH, especially over North America and Eurasia. A local warming in the Nordic Sea is induced by a stronger southwest wind blowing across the relatively warmer surface of the North Atlantic Ocean. In boreal summer, the key feature of 57.5 ka and 45 ka BP are a general

warming of up to 2.5 ^{0}C; close to North Atlantic Ocean that finds greater expression over the continents of the NH in JJA. It is clearly evident that increase of CO_2 concentration results in a global warming in both boreal winter and summer.

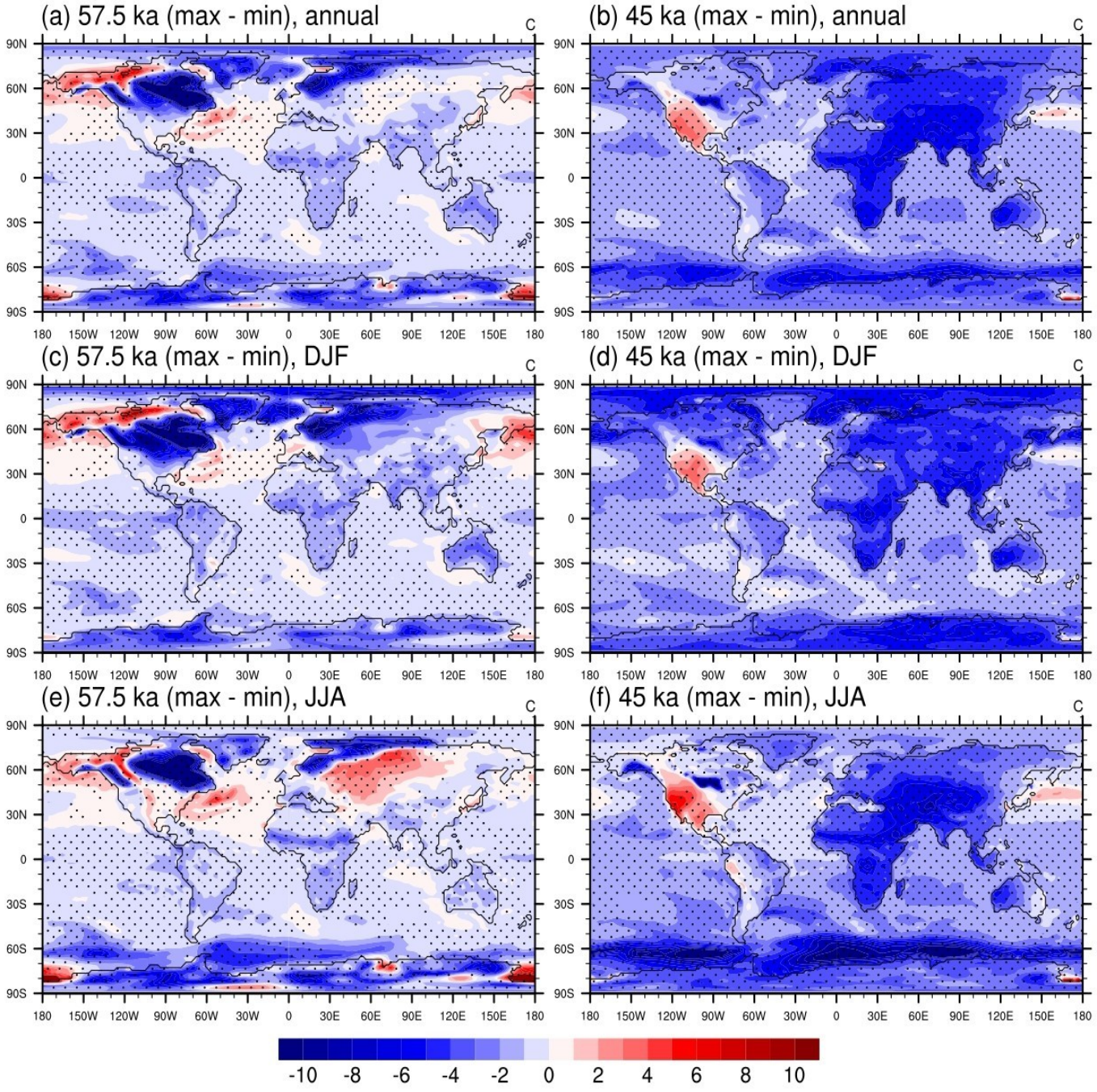

Figure 3.1. Simulated 2m surface temperature anomalies of MIS 3 maximal relative to their corresponding minimal ice sheet scenario with their respective land sea mask (coastline) for annual mean (a, b) and seasonal mean: winter - DJF (December–January February) (c, d) and summer - JJA (June–July–August) (e, f). The marked area has a significance level of above 95% based on Student's t-test. Units are ^{0}C.

3.2 Geopotential Height and Wind Circulation

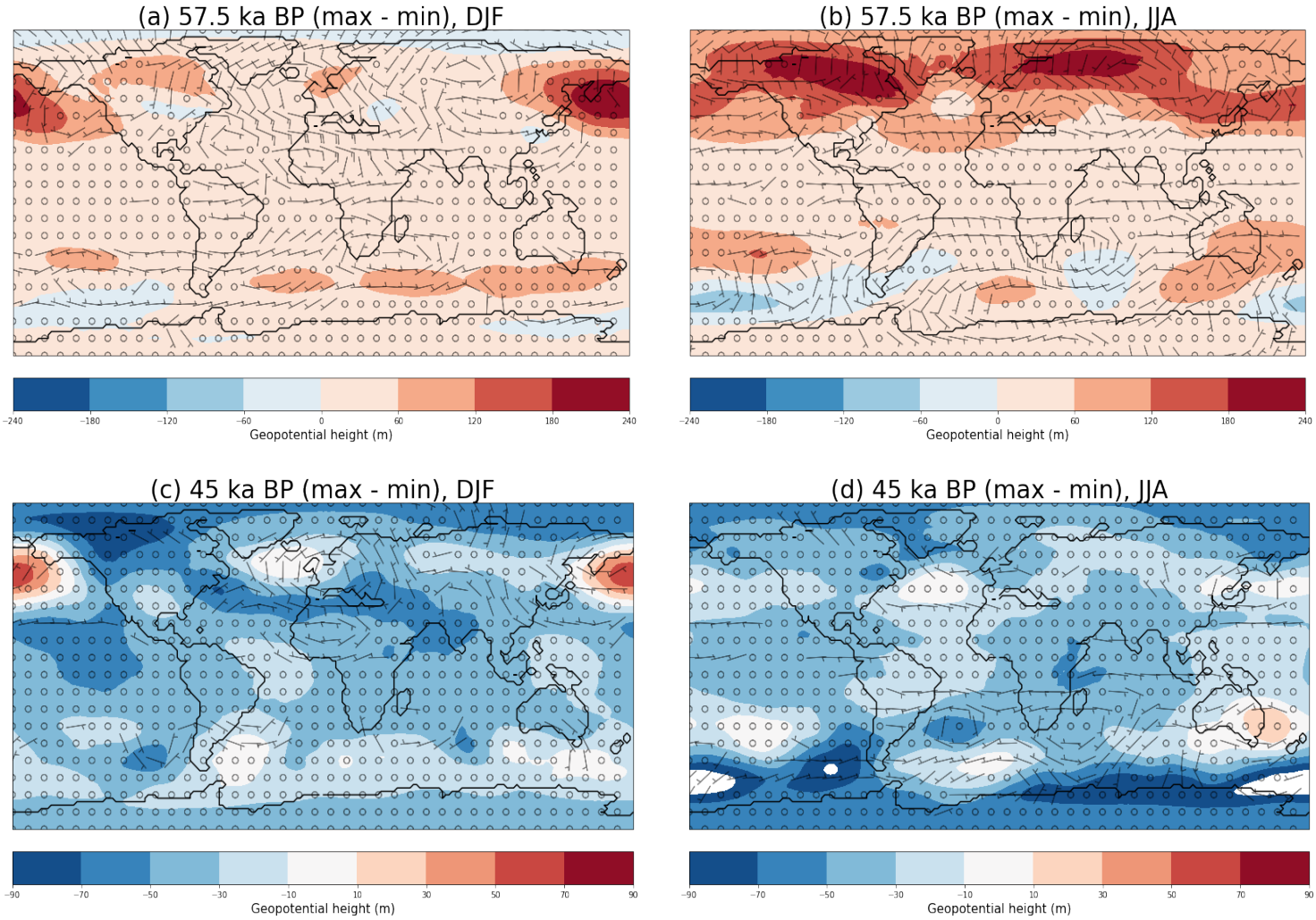

Figure 3.2. Simulated 500 hpa geopotential height anomalies (m), Land – sea mask (coastline) and wind barb anomalies (kt) of MIS 3 maximal relative to minimal scenario for seasonal mean; (a, c) winter - DJF and (b, d) summer - JJA.

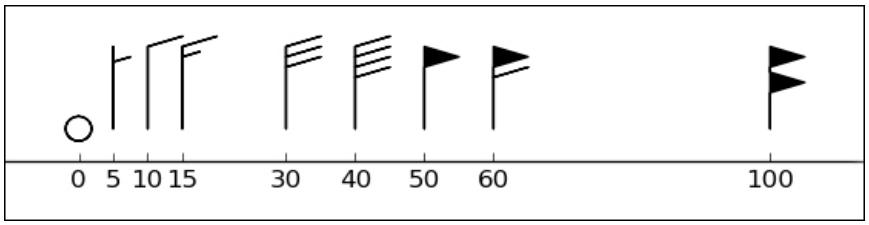

Figure 3.2.1. Wind barbs in knots, where 1 knot is 1.9 km/hr.

As shown in Fig. 3.2, the 500 hpa geopotential height (on average this level is around 5.5 km above sea level) and wind speed anomalies of MIS 3 (maximal – minimal) over NH, in 57.5 ka BP show stronger seasonal polar easter & westerlies than in 45 ka BP. The MIS 3 Laurentide Ice Sheet's elevated surface modifies atmospheric stationary waves, resulting in an enhanced, meandering wave pattern near the North American continent (Fig. A.5, A.6); the displayed 500 hpa geopotential height in winter shows enhanced troughs in the northwest Pacific and eastern Canada, as well as enhanced ridges in western Canada. The zonal wind reveals a stronger, more zonal, more northward shifted (by 4 degrees latitude) subpolar jet above the North Atlantic (not shown). As shown in Fig. 3.2, the cyclonic wind anomaly advects warm air to Alaska, contributing to diminished cooling. The Icelandic Low and Azores High migrate southwestward across the Atlantic, resulting in broader, stronger, and more southerly westerlies throughout the North Atlantic. Wind anomalies caused by ice sheets in the North Atlantic are a common characteristic in PMIP3 LGM simulations (Muglia and Schmittner, 2015). In the NH, mid and high latitudes, Greenland and LIS of the 57.5 ka, 45 ka BP and PI Greenlandic ice sheet modify the atmospheric stationary waves, and an enhanced wave pattern over the North American and European continent (Fig. A.5, A.6).

3.3 Total Precipitation

MIS 3 maximal anomalies of the annual and seasonal mean precipitation amount relative to the minimal scenario climate are shown in (Fig. 3.3). The summer monsoon in tropical Africa and southern India are intensified due to higher land-sea thermal contrast. These features are likely due to the precessional effect, since significant warming over the Northern Hemisphere continents occurs in experiment of MIS 3 when boreal summer is at perihelion. In contrast to the surface temperature anomalies, the precipitation anomalies follow diverse spatial patterns during MIS 3. The lowest precipitation anomalies are detected in the tropic regions of both East Pacific (up to 100 mm/month) & West Pacific (up to 80 mm/month) Ocean in 57.5 ka BP and also in the Indian Ocean during 45 ka BP (maximal - minimal) scenario, respectively. However, the precipitation significantly

decreases in some regions such as south-east of Asia, and in the NH over the centre of the North Atlantic, and North America. In general, the anomalies slightly decrease from around 40 degree polewards in 45 ka (maximal - minimal) but during 57.5 ka BP (maximal - minimal) over the North Atlantic Ocean (underneath of Greenland) precipitation is seen higher by 30 mm/month. The rainfall can be seen higher over the area, close to Labrador Sea, tropical regions and in Indian Ocean (only in 57.5 ka BP; maximal - minimal) and Atlantic Ocean during the boreal summer than the winter and annual mean. In the glacial MIS 3 climate, simulated annual precipitation is less, with both seasonal and geographical changes including a southward shift of the Intertropical Convergence Zone (ITCZ) compared to that in PI (Fig. A.7, A.8). In boreal winter, the significant decreases of precipitation are also seen at higher latitudes, where cold & dry conditions and extensive sea ice weaken the hydrological cycle in comparison with the warmer conditions of the PI. The only exception is found in parts of the tropics specially over the north Indian Ocean and Southeast Asian countries, where more precipitations are simulated during winter monsoons than summer and annual, which is associated with the ITCZ. However summer monsoons most raining regions are Sahel zone and the north Indian Ocean. Such monsoons are caused by the land-sea pressure and temperature contrast, which strengthens the moist onshore inflow to the land.

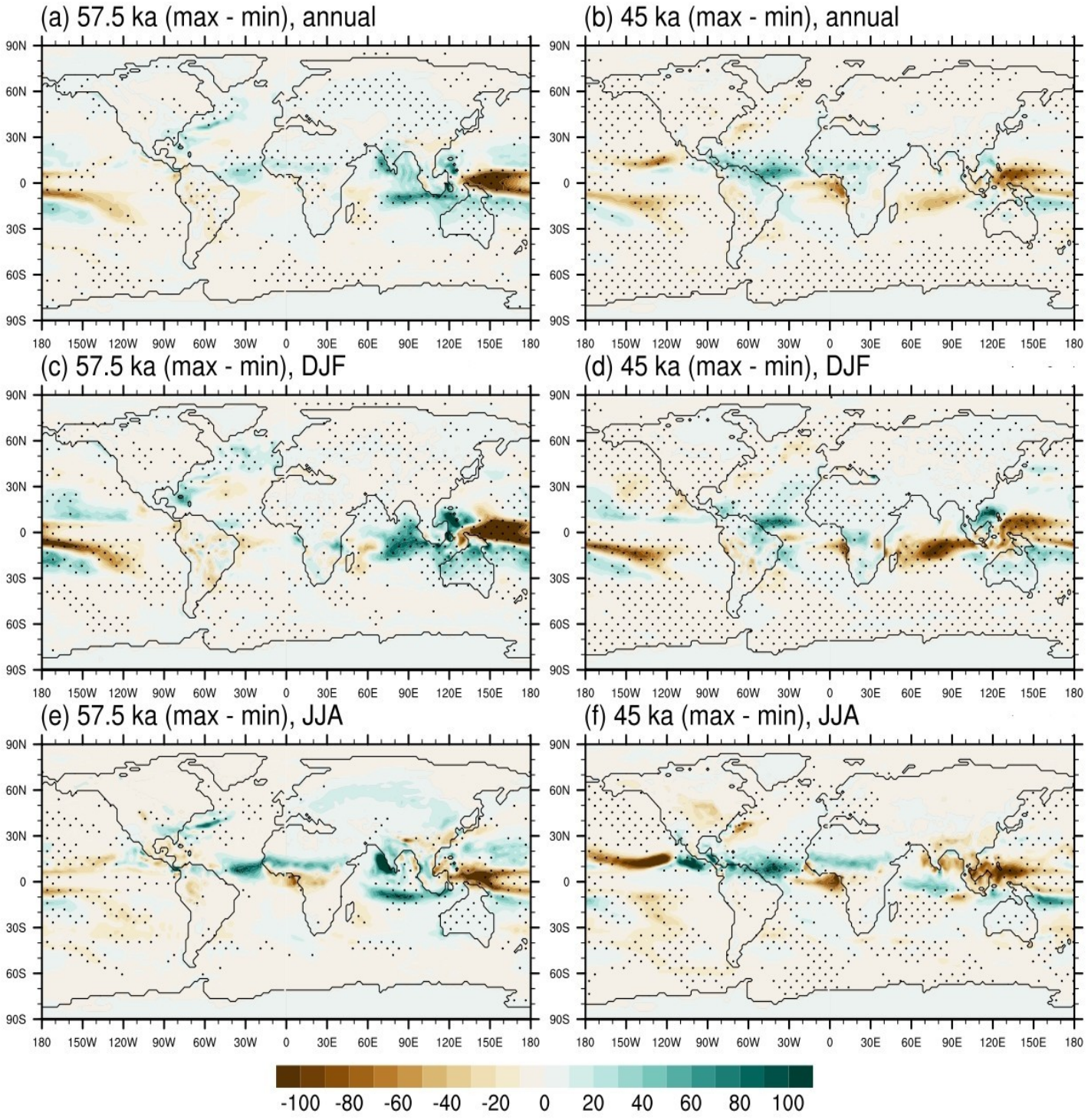

Figure 3.3. Simulated total precipitation anomalies of MIS 3 maximal relative to their corresponding minimal ice sheet scenario with their respective land sea mask (coastline) for annual mean (a, b) and seasonal mean: winter - DJF (c, d) and summer - JJA (e, f). The marked area has a significance level of above 95% based on Student's t-test. Units are mm/ month.

3.4 Sea Ice Concentration

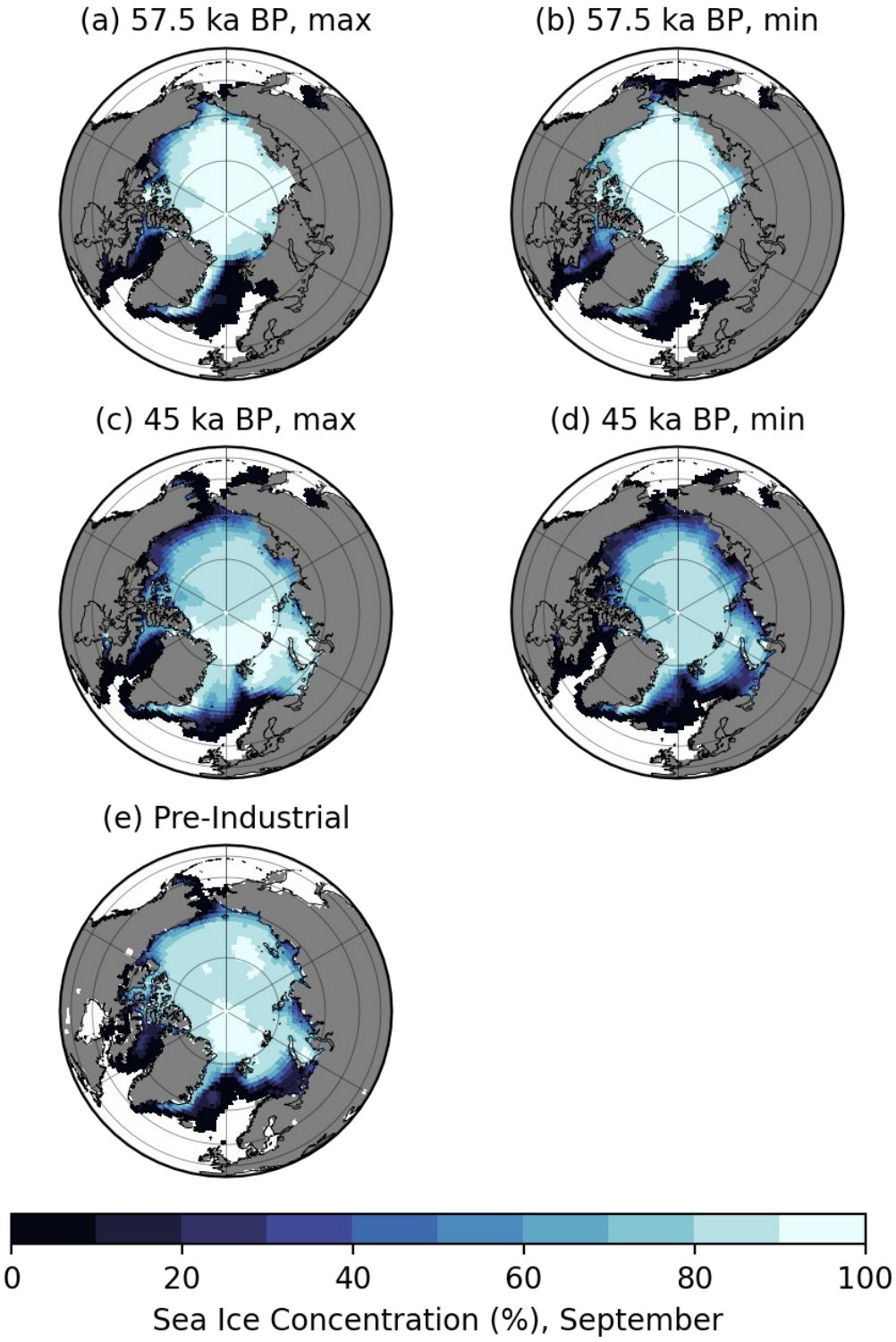

Figure 3.4. Simulated sea ice concentration in MIS 3 and PI with their respective land sea mask (grey shading) in September (summer) in NH: maximal (a, c), minimal scenario (b, d) and (e) PI. Units are %.

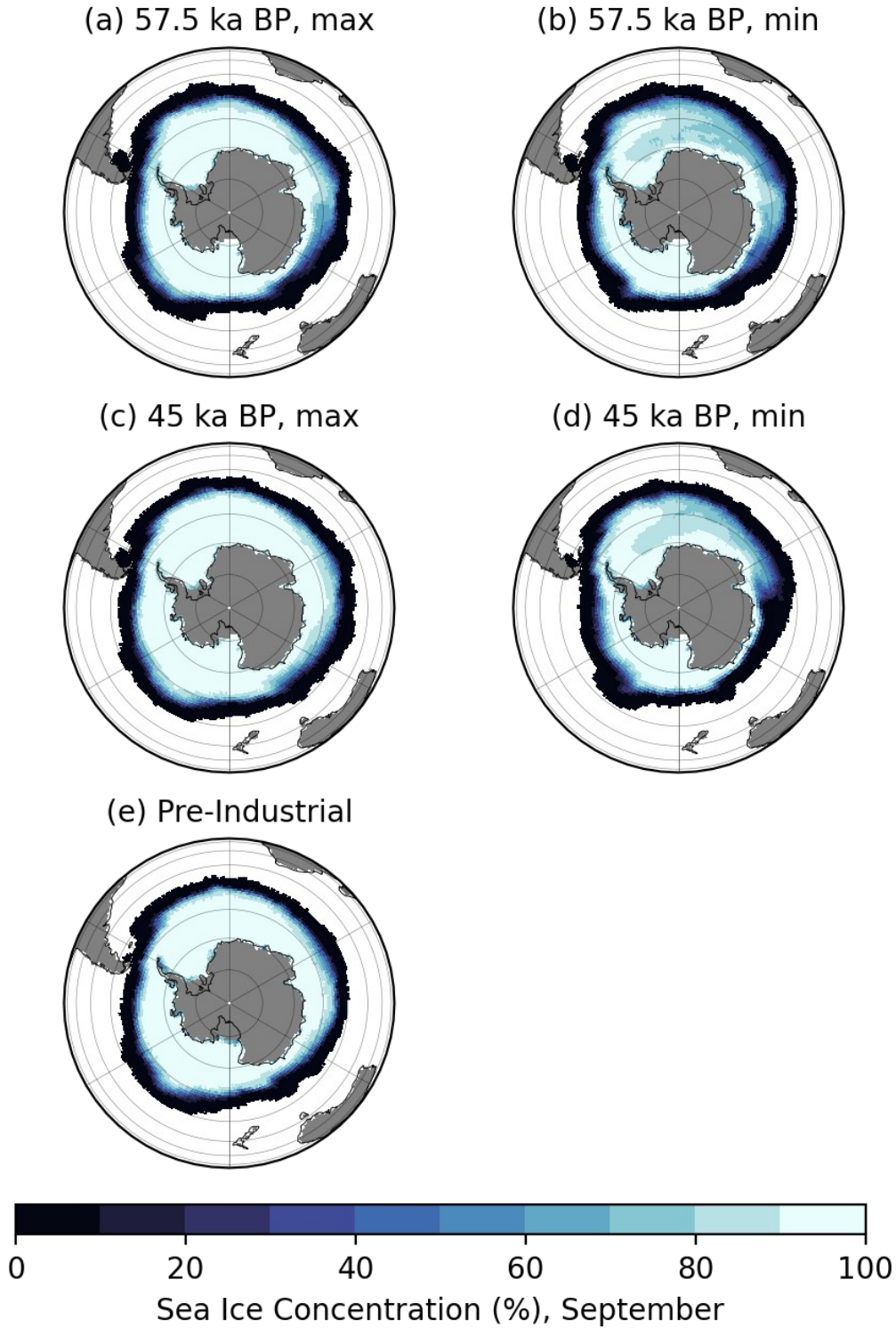

Figure 3.5. Simulated sea ice concentration in MIS 3 and PI with their respective land sea mask (grey shading) in September (summer) in SH: maximal (a, c), minimal scenario (b, d) and (e) PI. Units are %.

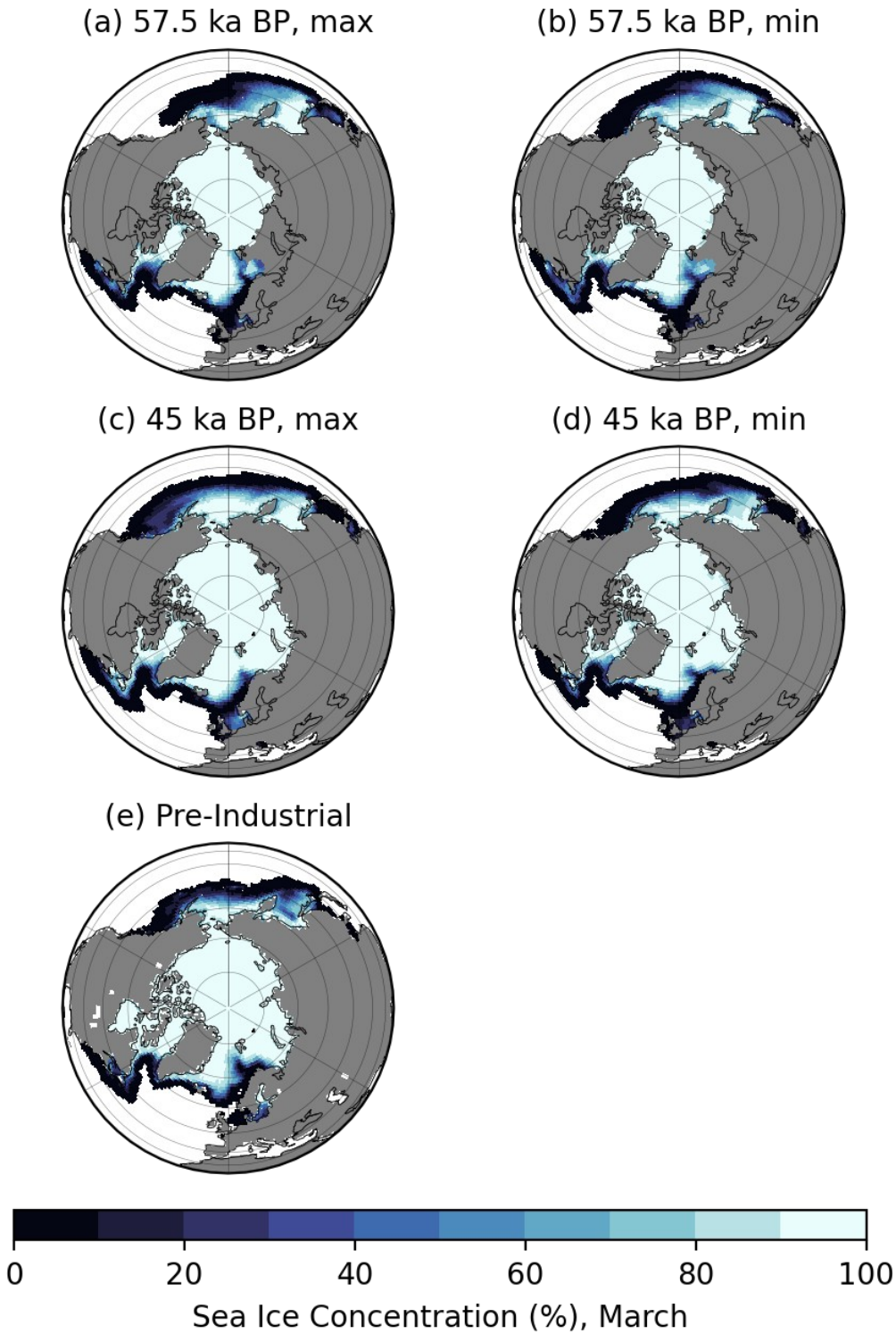

Figure 3.6. Simulated sea ice concentration in MIS 3 and PI with their respective land sea mask (grey shading) in March (winter) in NH: maximal (a, c), minimal scenario (b, d) and (e) PI. Units are %.

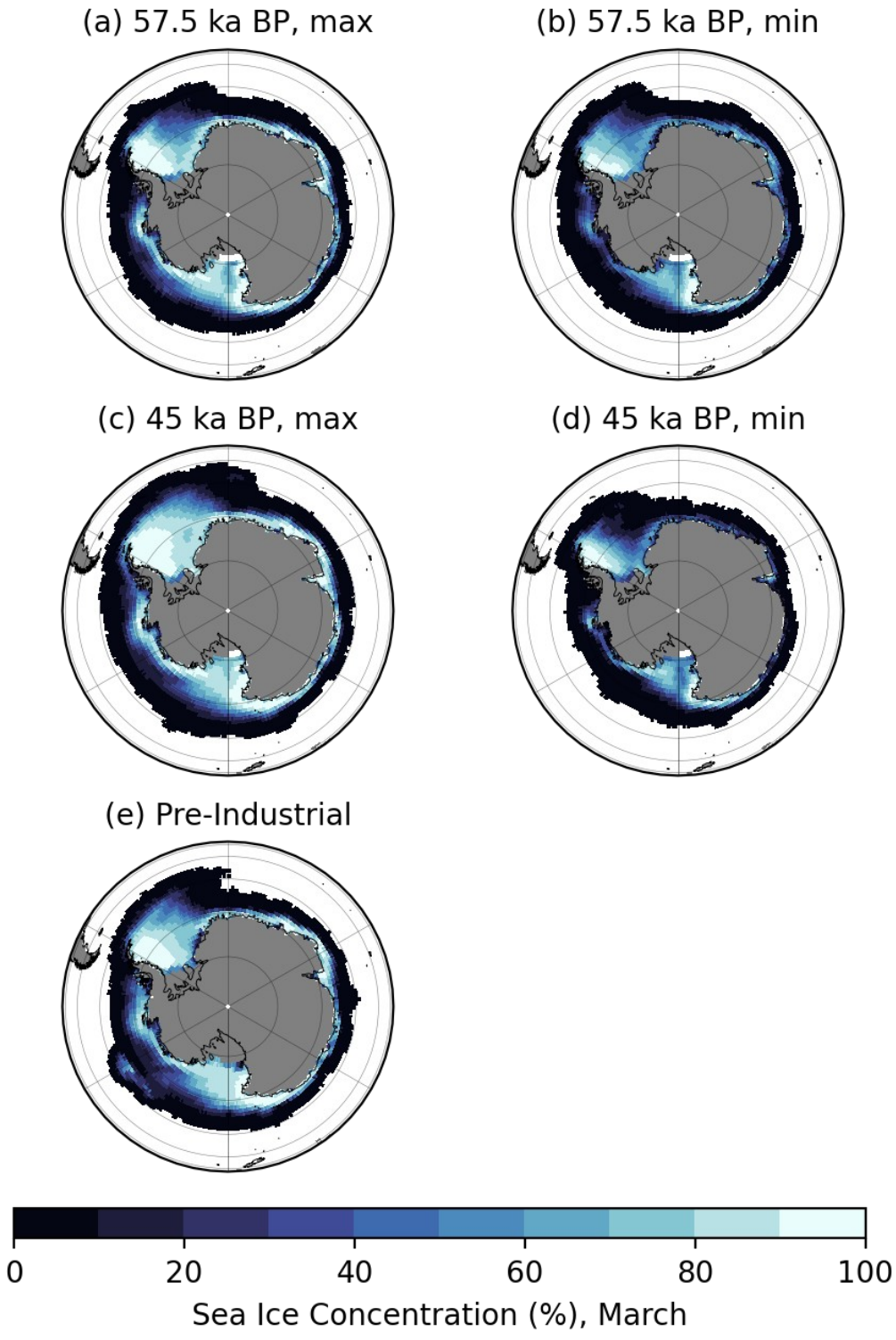

Figure 3.7. Simulated sea ice concentration in MIS 3 and PI with their respective land sea mask (grey shading) in March (winter) in SH: maximal (a, c), minimal scenario (b, d) and (e) PI. Units are %.

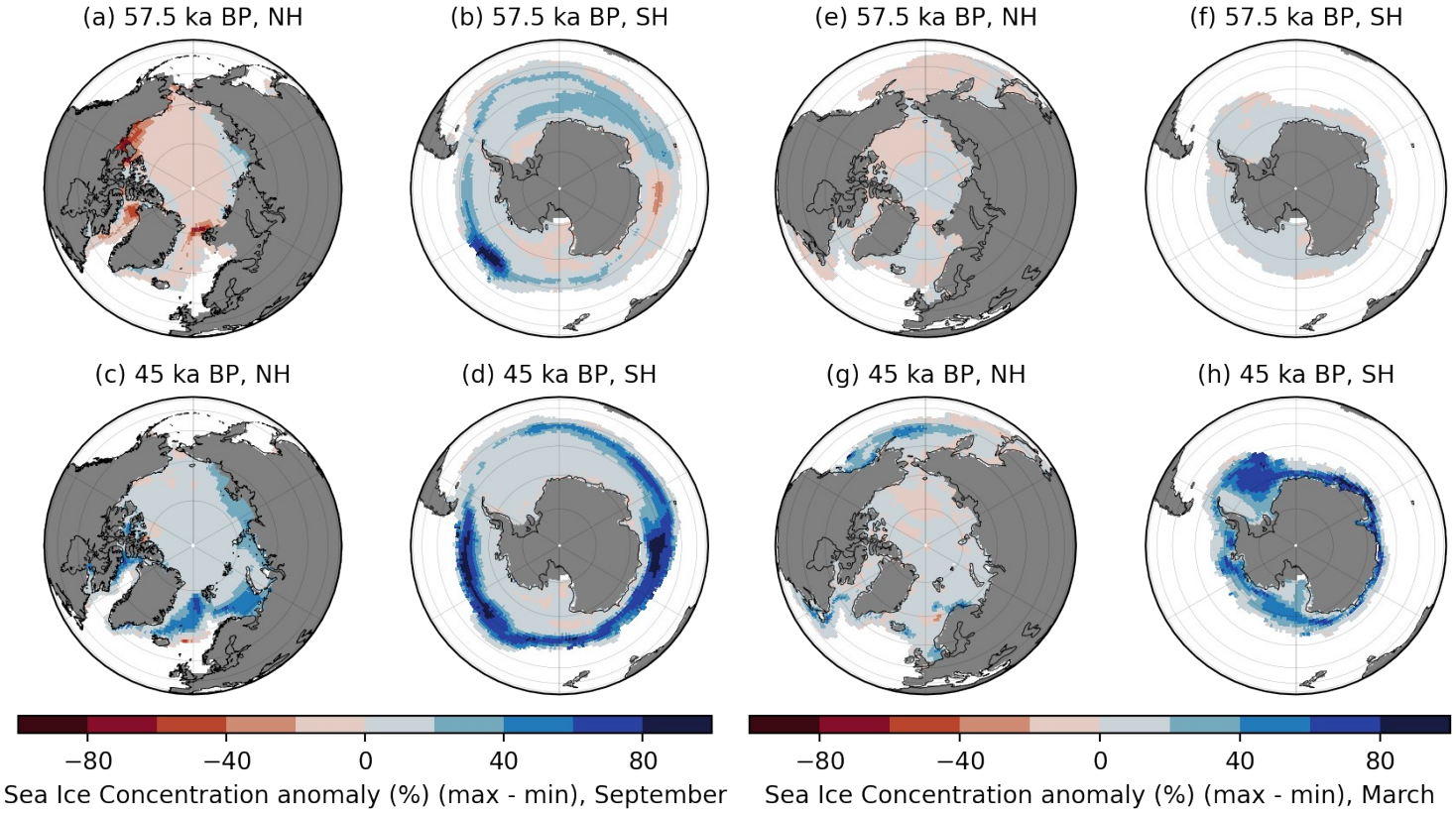

Figure 3.8. Simulated sea ice concentration anomalies of MIS 3 maximal relative to their corresponding minimal scenario with their respective land sea mask (grey shading) for seasonal mean (a, b): September - summer (a, b, c, d) March - winter (e, f, g, h). Units are %.

The simulated seasonal mean (September as summer and March as winter) of MIS 3 maximal and minimal sea ice concentration are shown in Fig. 3.4-3.7 and maximal relative to minimal anomalies are depicted in Fig. 3.8. The reduced atmospheric GHGs concentration during MIS 3 causes a lowering of SST and an expansion of sea ice. Sea ice cover contributed to an MIS 3 maximal climate different from minimal scenario and PI. At the higher latitude oceans, sea-ice in 45 ka BP-minimal was less extensive under elevated atmospheric temperatures (T_{2m}) and SSTs than 45 ka BP-maximal on the other hand in 57.5 ka BP-minimal shows more extensive sea ice than 57.5 ka BP-maximal. Poleward retreat of sea-ice involved a promotion in both local and global albedo, which further enhanced the cooling in MIS 3. In the Labrador Sea (up to 40 %) and Nordic Seas (up to 90 %) sea-ice are strongly increased, both in winter (March) and summer (September) in both hemispheres and scenario. Therefore, deep convection near the sea-ice margin could shift from the open waters of the North Atlantic to these regions. Where NADW production took

place, local additional surface heating resulted. In 57.5 ka BP, simulated maximal sea ice shows a drop compared to minimal sea ice and reason could be the increased surface temperature and SST over the North Atlantic and Pacific Ocean (Fig. 3.6), whereas in 45 ka BP, it exhibits positive sea ice anomalies (Fig. 3.8). In the Atlantic during MIS 3, in March there is more sea ice south of Newfoundland and in the northeastern Labrador Sea. However, there is less sea ice in the western Labrador Sea, which is likely due to the strong northerly katabatic wind induced by the presence of the adjacent LIS (Fig. 2.3) that moves the ice away. The Nordic Seas are partly ice-covered due to the intrusion of warm Atlantic water across the Iceland–Scotland ridge, with sea ice present off the coast of Norway in March. However, the central part of the Nordic Seas is ice full even in September (summer). Greater sea ice extent is found along the coast of south Greenland and in the Nordic Seas. The Barents Sea is fully ice-covered also in September at MIS 3 relative to PI. In the SH, MIS 3 shows extended Antarctic sea ice cover in both seasons. Furthermore, sea ice concentration is higher during MIS 3 relative to PI, especially in the Weddell Sea region.

3.5 Sea Surface Temperature

The response of sea surface temperature (SST) to MIS 3 maximal relative to minimal insolation and GHGs are shown in Fig. 3.9. The model produces a general global cooling, especially across the tropical and subtropical regions, induced mostly by reduced insolation in boreal winter. The reduced atmospheric CO_2 concentration during MIS 3 causes a lowering of SST and an expansion of sea ice. The geographical distribution of the cooling reflects the change in surface air temperature, as shown in Fig. 3.1. The annual and summer mean distribution of SST anomalies are characterized by a warming over the North Atlantic Ocean, North Pacific Ocean, Baffin Bay and Nordic Sea (up to 3 ^{0}C) in 57.5 ka BP (maximal – minimal), on the other side in 45 ka BP (maximal - minimal) cooling (up to 4 ^{0}C) can be seen globally except over some areas of north-east Pacific Ocean. It is attributed mainly to increased insolation in boreal summer, which is induced by a larger tilt of the

orbital plane. The most intriguing change happens over the Gulf Stream, where the largest SST gradient occurs.

Simulated both DJF (winter) and JJA(summer) mean of MIS 3 SST is colder up to 4 ^{0}C with respect to the PI (Fig. A.9). The cooling is relatively modest up to 3 to 4 ^{0}C in the tropical and subtropical oceans, and increases towards higher latitudes, in particular in the North Pacific, the Barents Sea, the Nordic Sea, and the Southern Ocean. In contrast, the central North Atlantic exhibits less cooling and even exhibits warming near the centre of the subpolar gyre, relatively weak cooling in the North Atlantic subpolar region is likely caused by a stronger ocean circulation (AMOC) bringing more ocean heat from the tropics to this region.

Table 3.2: Global mean values for the MIS 3 maximal relative to minimal ice sheet scenario experiments.

Simulation	**T_{2m} (^{0}C) ≈**	**Precipitation (mm/month) ≈**	**Sea ice concentration (%) ≈**	**SST (^{0}C) ≈**
57.5 ka BP (maximal - minimal)	-1.14	+0.36	+1.60	-0.36
45 ka BP (maximal - minimal)	-2.31	+3.81	+3.10	-1.36

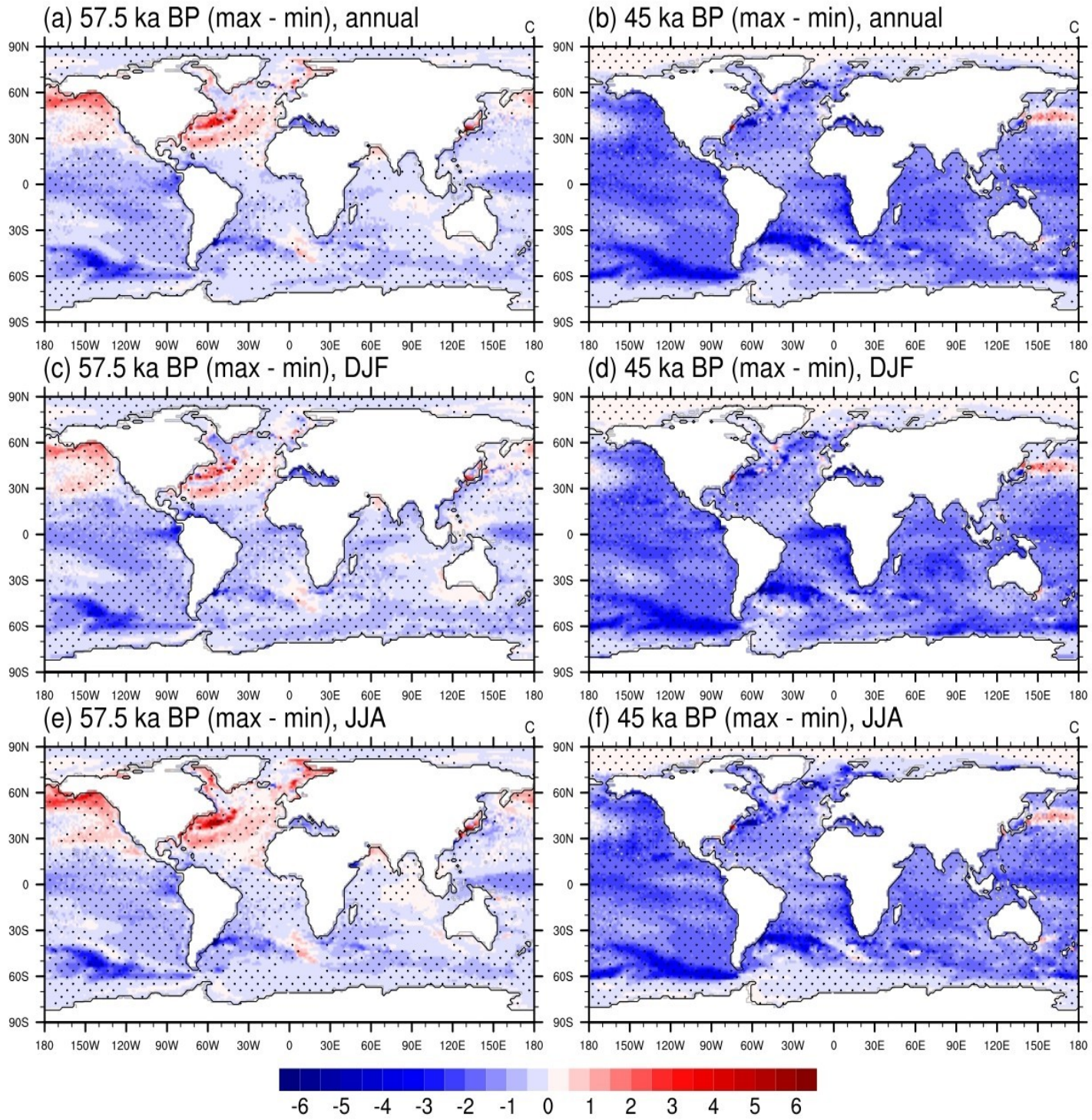

Figure 3.9. Simulated sea surface temperature anomalies of MIS 3 maximal relative to their corresponding minimal ice sheet scenario with their respective land sea mask (grey shading) for annual mean (a, b) and seasonal mean: winter - DJF (c, d) and summer - JJA (e, f). The marked area has a significance level of above 95% based on Student's t-test. Units are ^{0}C.

3.6 Atlantic Meridional Overturning Circulation (AMOC)

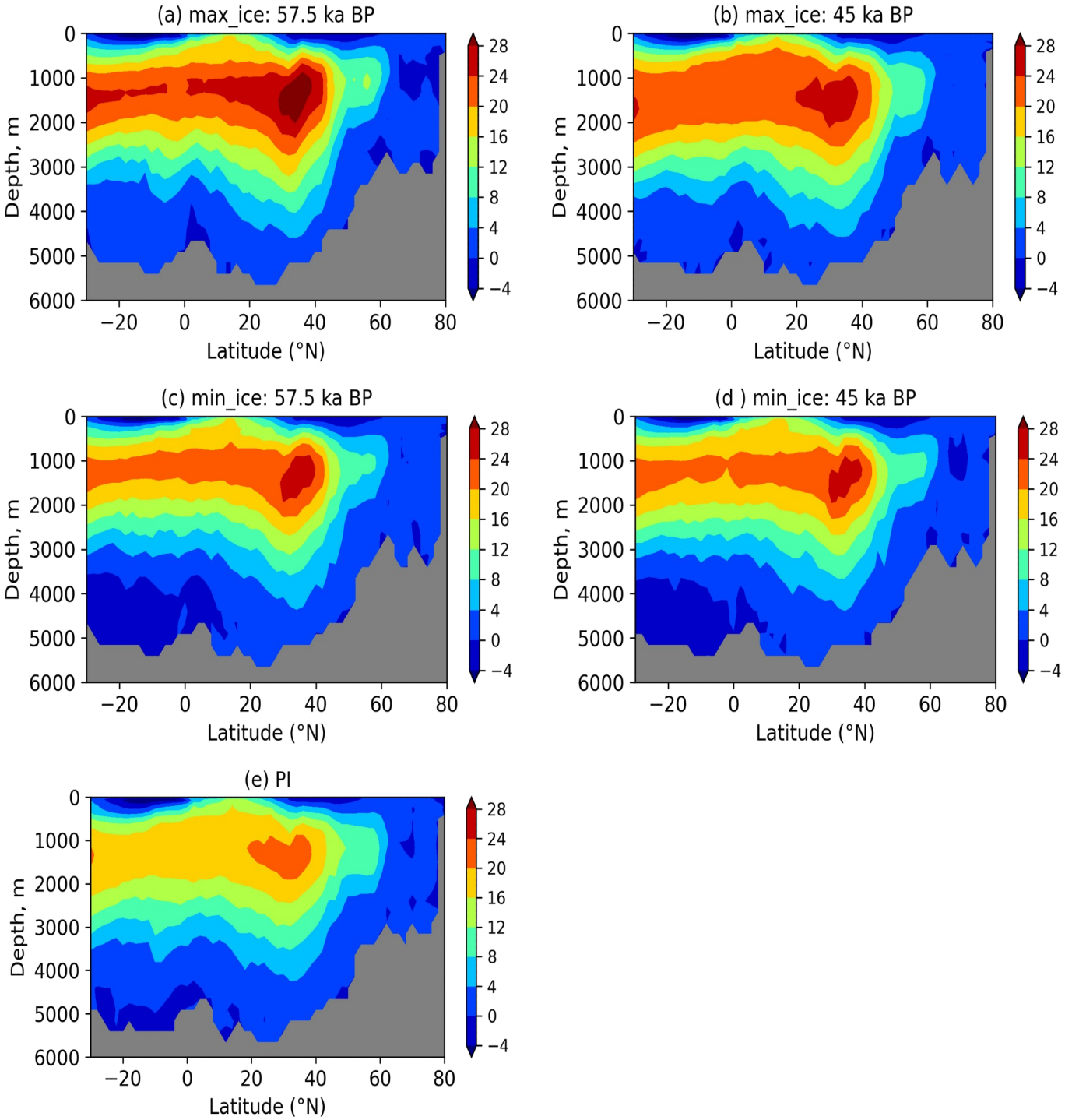

Figure 3.10. Simulated annual mean AMOC. The last 100 year average of model run in MIS 3. (a, b) 57.5 ka & 45 ka BP maximal, (c, d) 57.5 ka & 45 ka BP minimal and (e) PI simulation. We can see a strong, upper circulation cell, transporting water from the high latitudes toward the south. Units are Sv.

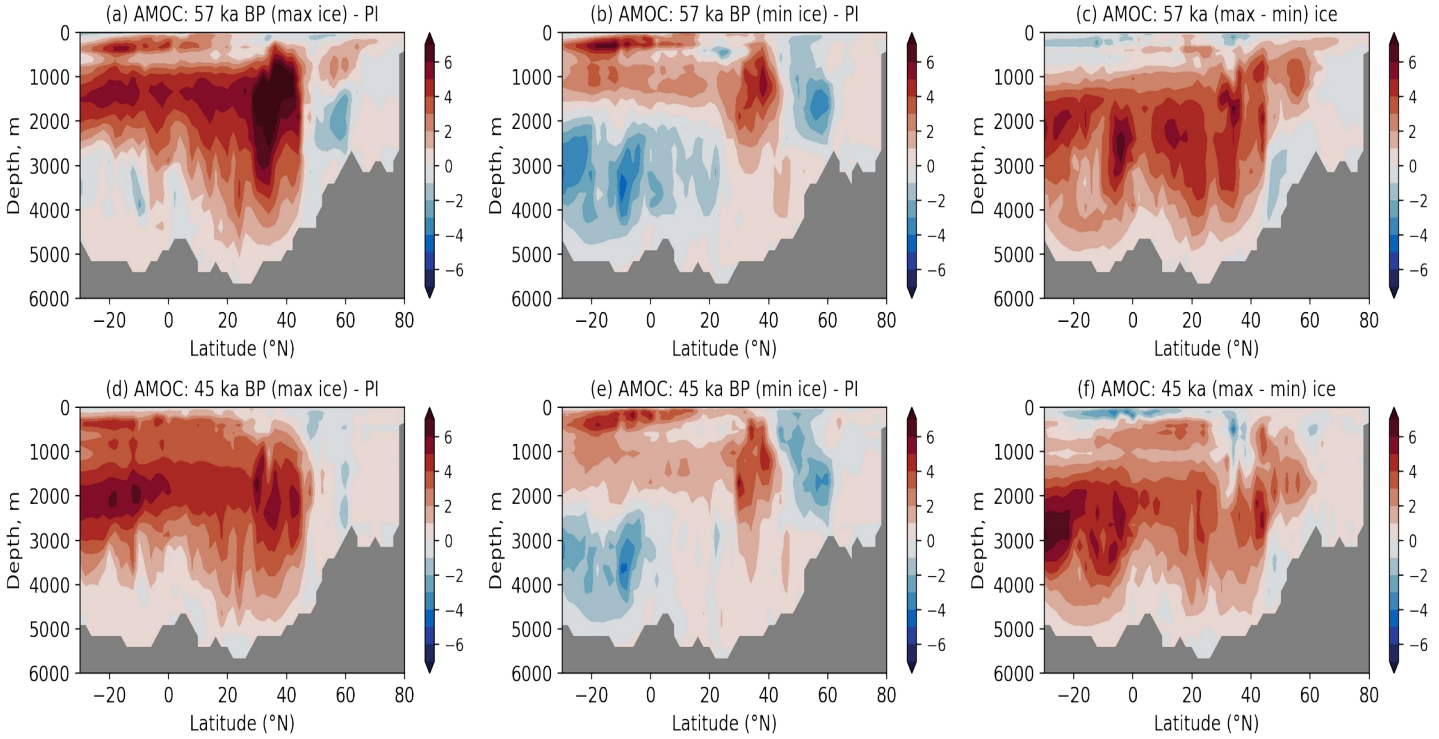

Figure 3.11. Simulated annual mean AMOC anomalies of MIS 3 (57.5 ka & 45 ka) BP- maximal and minimal scenario relative to PI simulation (a, b, d, e), and maximal – minimal (c, f). Units are Sv.

The North Atlantic Ocean is a critical region for the AMOC since its variability can change sea-water properties in particular the density in the sinking region of the North Atlantic deep water formation sites and thus affects the strength of the AMOC. Abrupt climate changes such as D-O events have been shown to involve changes in both the geometry and strength of the AMOC, as indicated by a number of marine proxy reconstructions (Lynch-Stieglitz, 2017) and numerical simulations (Peltier and Vettoretti, 2014; Brown and Galbraith, 2016). In this section, a stronger and deeper AMOC is simulated during a typical MIS 3 (maximal and minimal scenario) as compared to the PI and maximal relative to minimal scenario (Fig. 3.10, 3.11). In comparison to minimal and PI, the AMOC in MIS 3 of the maximal ice sheet scenario is stronger due to the higher volume of the ice sheet than minimal scenario and PI which are caused the ocean water body more saline.

The AMOC stream function – defined as the zonally integrated transport over the Atlantic basin – has respective averaged value of about and 15.4 Sv (1 Sv = 10^6 m^3 /s) in the PI experiment. Compared with the corresponding PI state, the strength of the AMOC increases by up to 5 Sv in maximal and minimal, respectively (Fig. 3.11. a-e). The AMOC over the Atlantic basin, has the maximum of up to 28 Sv at 1000 to 2000 m depth of 35 ^{0}N to 40 ^{0}N (Fig. 3.10) in MIS 3 in both scenarios. The AWI-ESM-2.1 experiments show strengthened AMOC at MIS 3 (~27.5 Sv) relative to the PI (~24.3 Sv). The depth of the AMOC maximum for MIS 3 is unchanged and located at 800 m. Regarding the behavior of MIS 3 maximal relative to minimal AMOC, the maximal scenario of MIS 3 AMOC stream function shows stronger of between 1000 to 4000 m depth between 20 ^{0}N and 40 ^{0}N, with the magnitude of between 2 to 4 Sv, respectively (Fig. 3.11. c, f). The deep overturning cell associated with Antarctic Bottom Water (AABW) is contracted and weakened. Zhang et al., 2014b reported a similar strengthening of AMOC during MIS 3 (boundary conditions), e.g. ~15.4 Sv, which is ~1.5 Sv stronger than their PI control simulation but is much weaker than my simulated strength of AMOC at MIS 3. Enhanced upward mobility of sea water away from sinking regions is expected during MIS 3 due to more vigorous deep water creation in the NH (related with a stronger AMOC) and in the SH (Munk, 1966). This leads to a thermocline that is displaced upwards with a sharper vertical gradient, contributing to the cold anomaly near the base of the thermocline. Similar upward displacement of the thermocline and an associated cold anomaly are also seen in the Pacific Ocean (not shown) is primarily caused by reduced warm Mediterranean outflow during MIS 3.

Chapter 4

Discussion

In this chapter, a discussion of MIS 3 response to different forcing and boundary conditions are presented. Analyses of the MIS 3 (maximal and minimal scenario) experimental results as simulated by AWI-ESM-2.1, as well as comparison of maximal and minimal results are also discussed. Furthermore, evaluation of AMOC is discussed. The discussion concludes with an assessment of results obtained for climate oscillation under different forcings and boundary conditions.

4.1 Model Resolution

Model resolution is an important factor in climate models, as models with different resolutions can obtain opposite climatic responses to a given forcing (Shi and Lohmann, 2016). Traditional simulations of the paleoclimate are mostly based on relatively coarse resolutions in which a number of important small-scale processes, such as eddies and topographically influenced ocean currents, may not be presented explicitly. In simulations I apply a state-of-the-art, low-resolution model, AWI-ESM-2.1, to simulations of the MIS 3 (maximal and minimal scenario). I apply an unstructured ocean grid with resolution varying from about 20 km in the Arctic (north of 50°N) and in the tropics (around 0°N) to about 150 km in parts of the open ocean. The ice–ocean component, FESOM-2.0, has the advantage of offering a regional focus within a global setup (Sidorenko et al., 2019). In principle, such a multi-resolution approach allows to use enhanced horizontal resolution in dynamically active regions while otherwise keeping a coarse resolution setup otherwise (Sidorenko et al., 2019). The model has been validated in previous studies indicating good agreement between the modeled and the observational mean fields.

4.2 Comparison of simulated MIS 3-maximal and MIS 3-minimal climates

Similar to my simulation results, enhanced MIS 3 seasonality has been found in observations. For example, proxy data indicate a boreal summer cooling in northern Canada, northeastern and northwestern Europe, and central-west Siberia (Davis et al., 2003; Zhang et al., 2018). Moreover, carbon and oxygen isotopes document a warming during the boreal winter season over NH continental in summer of MIS 3 in 57.5 ka BP maximal relative to minimal scenario (Fig. 3.1) and globally cooling with respect to PI (Fig. A.1). The simulated annual global mean T_{2m} is ~2.31 ^{0}C cooler in MIS 3 maximal than during the minimal scenario in 45 ka BP and during 57.5 ka BP it shows in ~1.14 ^{0}C cooler, due to the atmospheric GHG concentrations relative to PI and less extensive continental ice sheets and sea ice cover relative to minimal scenario.

Besides higher summer-season insolation, the deglacial warming (57.5 ka BP) over the North Atlantic and the Pacific Ocean and glacial cooling in 45 ka BP, also stems from climate-system-internal processes such as progressive invasion of warm Atlantic waters into this basin and changes in the oceanic conveyor belt (Fig. 3.9). In this study, the simulations forced by 57.5 ka BP insolation and GHGs are able to capture such warming might be the reason of quite similar ice sheets volume size in between 57.5 ka maximal and minimal scenario (Fig. 2.3); while other, with 45 ka BP topography and ice sheets applied, show a cooling at various magnitudes. The reason behind such model behavior possibly lies on the fact that the cooling effect of LIS and CIS are overestimated in the model. The fresh surface water in the South China Sea during MIS 3 is caused by increased runoff from the new river routing in this region due to the change of land–sea mask. In the southwest Pacific, surface freshening is due to a southward shift of the ITCZ and an overall decrease of evaporation minus precipitation in the region. Off the coast of Antarctica, enhanced formation of sea ice, and the associated brine release, leads to an increase in surface salinity; the effect is especially pronounced in the Weddell Sea region.

For the northern tropics of Africa, the desert retreat associated with enhanced precipitation signalise a northward shift and intensification of the intertropical convergence

or a combination of both. In case of a northward shift, the increased precipitation in the northern tropics is accounted for, but the precipitation does not change over the southern tropics. In the case of intertropical convergence intensification, an increase in rainfall is expected on both sides of the ITCZ, which is not the case for the southern side. We argue for a combination of both in a warmer climate with more vigorous NH warming.

The second external factor causing the colder MIS 3 conditions was the enhanced surface albedo due to larger ice sheets (Gowan et al., 2021) and more extensive sea-ice cover (Fig. 3.4, 3.6). More extensive continental ice cover causes the surface albedo to increase, while higher ice sheet topography directly decreases local T_{2m} and therefore the global mean SST. As can be expected, with small differences in ice sheets and topography forcing, the MIS 3-maximal and MIS 3-minimal simulations feature virtually the different climate. This implies that differences in atmospheric GHG and dust forcings during MIS 3 did not affect the temperatures in the same order of magnitude as ice sheet and orbital configuration do. In MIS 3 maximal experiment, the global sea surface temperature cools by ~0.36 ^{0}C (~1.36 ^{0}C) relative to MIS 3 minimal experiment in 57.5 ka BP (45 ka BP), respectively (Fig. 3.9). Winter sea ice slightly expands southwards in the Nordic Seas and in the northwestern Pacific, whereas in the Labrador Sea, sea ice distribution is nearly identical in MIS 3 experiments. Furthermore, there is a small change to the AMOC. Together, these results indicate that given the changes to the GHG levels that are typical of a stadial state, a cold Greenland climate with a weak AMOC cannot be reproduced in my MIS 3 setup without additional freshwater forcing.

The AWI-ESM-2.1, MIS 3 experiments exhibit surprising stability without any significant changes in Greenland temperature, sea ice, or AMOC (Fig. 3.10). For the low CO_2 experiments, there is a slight expansion of winter sea ice in the Nordic Seas (Fig. 3.4, 3.6), without any notable changes in the strength and locations of convection. As a consequence, the AMOC, although weakened, still remains strong. For the experiments with a reduced LIS, surface wind stress fields are altered (mainly shifting northwards in the North Atlantic; not shown), whereas the strength of AMOC is only slightly reduced.

4.3 Simulated AMOC response

The AMOC during MIS 3 simulations presented here is associated with an annual mean sea ice expansion in the Nordic Seas (Fig. 3.10). Nevertheless, the western parts of the Nordic Seas are ice free in NH summer in MIS 3 simulation. These changes present two competing effects on the deep water production in the Nordic Seas. The increased sea ice extent inhibits heat flux from the ocean to the atmosphere, which would cool and thus increase the density of the surface waters in the Nordic Seas. The formation of sea ice during autumn and winter, on the other hand, leads to brine rejection, which results in increased density. I may conclude that the reduction of the AMOC found in the 45 ka than 57.5 ka BP simulation is in agreement with an increased sea ice expanse and that this effect dominates over the effect of increased brine rejection in the western Nordic Seas. In the coupled climate system the interaction between the ocean, sea ice, and atmospheric dynamics are non-linear and it is therefore difficult to identify cause and effect.

A number of marine proxy reconstructions (Lynch-Stieglitz, 2017) and numerical simulations (Peltier and Vettoretti, 2014; Brown and Galbraith, 2016) have shown that abrupt climate shifts, such as D-O events, include changes in both the shape and strength of the AMOC. When compared to the PI, a stronger and deeper AMOC is reproduced during a typical MIS 3 in this study (Fig. 3.10). Given its crucial role in the climate of MIS 3, I further discuss the simulated AMOC and the associated distribution of North Atlantic Deep Water (NADW) and AABW in this section. Previous research has suggested that higher AABW production during glacial periods is caused by extended Antarctic sea ice and greater brine rejection during the creation of sea ice in the Southern Ocean (Shin et al., 2003; Ferrari et al., 2014). The brine causes a negative buoyancy flux, resulting in more highly saline AABW formation. According to Jansen (2017), changes in deep ocean stratification and circulation are a direct result of atmospheric cooling during glacial periods, which causes Antarctic sea ice accumulation and initiates the processes detailed above. In comparison to the PI, the simulated ventilation of AABW is improved in MIS 3 simulation (Fig. 3.10). However, the volume of AABW produced in the Atlantic is not comparable to that produced during the LGM, when benthic foraminiferal C-13 data suggest that AABW

dominated the water column in the Atlantic up to a depth of 2 km (Curry and Oppo, 2005), along with shallower NADW production (Curry and Oppo, 2005).

While deep water production in the Southern Ocean has the potential to displace and reduce the strength of the NADW production, competing effects are at play in the North Atlantic. For example, the altered surface westerlies in the North Atlantic caused by the elevated LIS (Fig. 2.3) are shown to be able to induce a deeper and stronger AMOC by transporting more salt northward within an intensified gyre circulation, favouring deep ocean convection (Montoya and Levermann, 2008; Oka et al., 2012; Muglia and Schmittner, 2015; Klockmann et al., 2016; Sherriff-Tadano et al., 2018); the closure of Bering Strait leads to an increase of surface salinity in the North Atlantic thereby invigorating deep ocean convection and strengthening the AMOC (Hu et al., 2010, 2015). To isolate and assess the relative impact of these different processes requires a suite of dedicated sensitivity studies which is beyond the scope of this paper, but it is worth mentioning that the processes that take place in both hemispheres act together to create the AMOC shown in Fig. 3.10. During MIS 3, Sea level dropping and the elimination of shallow continental margins (Fig. 4.2) result in increased tidal dissipation in the open ocean (Egbert et al., 2004), implying enhanced deep ocean mixing and a strengthened AMOC. Schmittner et al., 2015 demonstrated that tidal impacts can outweigh surface buoyancy effects, resulting by ~40% increase in AMOC. The AMOC is projected to increase and deepen, perhaps displacing the lower AABW cell in the Atlantic, if such tidal impacts are taken into account in the current analysis.

For the lower CO_2 and ice sheets experiments, there is a slight expansion of winter sea ice in the Nordic Seas, without any notable changes in the strength and locations of convection. As a consequence, the AMOC, although weakened, still remains strong. For the experiments with a reduced LIS, surface wind stress fields are altered (mainly shifting northwards in the North Atlantic; not shown), whereas the strength of AMOC is only slightly reduced. In simulations, where the Labrador and Norwegian Seas are the major convection sites, a significant change of ocean circulations is not expected unless the Labrador and Norwegian Seas are covered by sea ice, thereby inhibiting convection through its insulating effect. However, the AWI-ESM-2.1 MIS 3 and PI experiments both appear to

be in a stable regime with a strong AMOC and strong convection in the Labrador and Norwegian Seas (Fig. A.9).

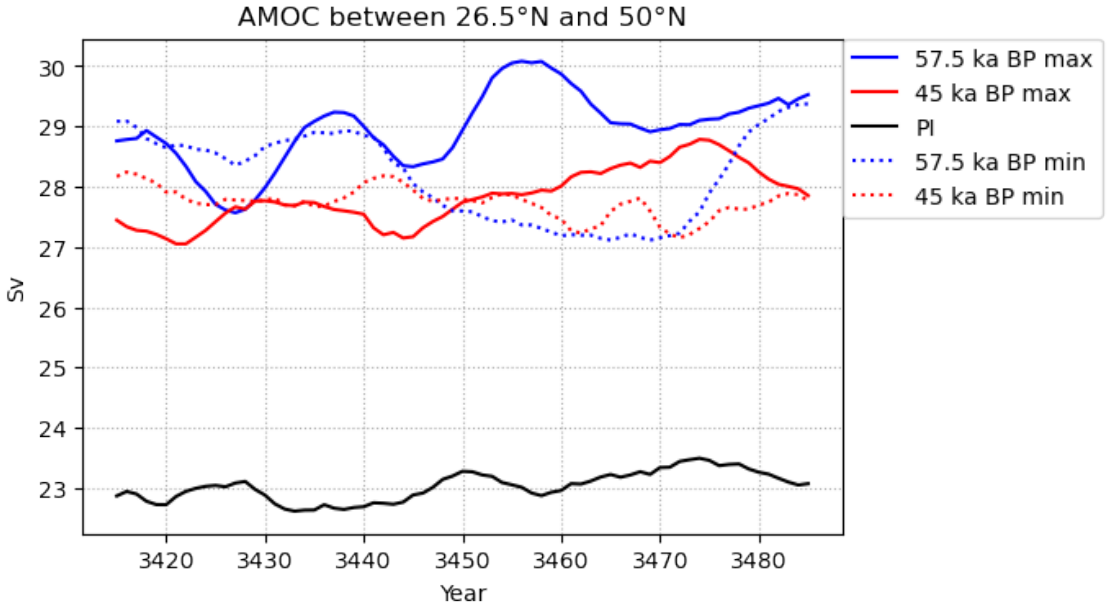

Figure 4.1. Time series of last 100 years of model run AMOC at between 26.5 ^{0}N and 50 ^{0}N for the experiments with maximal and minimal ice sheet scenario of MIS 3, and PI simulations. The sensitivity experiments are branched off from MIS 3 run at year 1500 and PI at year 1000.

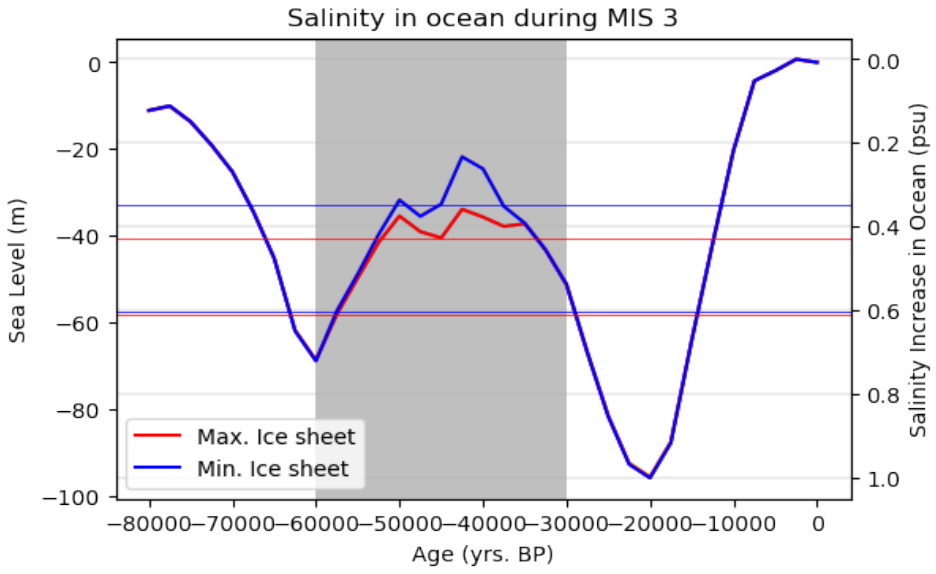

Figure 4.2. Relations between sea surface salinity and sea level in the 80 ka BP reconstruction. The blue line represents for minimal, while the red line is for maximal ice sheet scenario of MIS 3 (grey shading). Calculated ice-volume equivalent sea level, compared with the global sea water δ ^{18}O stack (blue line with 2σ error range), converted to sea level using a value of -116 m for the maximum sea level drop (Gowan et al., 2021).

From Fig. 4.2, In MIS 3 during the 57.5 ka BP maximal (minimal) ice sheet scenario, the ocean salinity is ~0.62 PSU (~0.61 PSU) PSU and sea level ~59 m (58 m) lower, and in 45 ka BP maximal (minimal) scenario salinity is ~0.43 PSU (~32 PSU) and sea level ~41 m (36 m) lower, respectively. Since the Eurasian Ice Sheets were generally restricted to mountainous areas during the middle of MIS 3, fluctuations in global sea level were controlled almost exclusively by the LIS (Fig. 2.3). GIA modelling studies confirmed that the sea level was higher than what was expected from ocean $\delta\ ^{18}O$ proxies, due to the reduction of the ice sheet. They predicted sea level as high as about -40 m. During much of MIS 3, the calculated sea level is consistent with this value. If Hudson Bay became ice free as in the minimal scenario, there would have been a sharp rise in sea level, which reached up to -25 m. It is unlikely that sea level could have remained as low as -60 m to -90 m as suggested in proxy-based reconstructions, as even my maximal reconstruction generally remains above -50 m between 50 ka and 35 ka BP (Gowan et al., 2021).

Chapter 5

Conclusion and Outlook

In this thesis, I have described the response of simulated oceanic and atmospheric circulation in the Northern Hemisphere to different MIS 3 (57.5 ka & 45 ka BP) forcings (including insolation and GHGs), boundary conditions (maximal and minimal ice sheet scnearios) and how they combine with changed topography and ice sheet (including the presence of LIS & CIS), for MIS 3-maximal relative to MIS 3-minimal ice sheet scenario. My results are based on integrations performed with the state-of-the-art model AWI- ESM-2.1 featuring a horizontal resolution of 1.9^0 in the atmosphere and 1.9^0 in the ocean with T63L47 set up. The fast performance of the model allows the experiments to be integrated for 1500 years. In thesis, I mainly focus on how surface properties and the AMOC respond to various MIS 3 forcings and the boundary conditions for maximal are notably different from the minimal due to changes in topography and the height and extent of the global ice sheets.

Orbital insolation forcing leads to enhanced Northern Hemisphere seasonality, with mainly warmer summers due to an increase of summer insolation, whereas winter insolation does not change substantially. The simulated 57.5 ka BP (45 ka BP)-maximal climate, global mean T_{2m} is ~1.14 ^{0}C (~2.31 ^{0}C) cooler than the 57.5 ka BP (45 ka BP)-maximal, repectively, with the borealwinter cooling (over the higher latitudes of NH and SH continents) especially above the LIS and CIS ice sheets and near the edges of the newly formed sea ice but boreal summer warming in NH (over the northern side of North America, Europe and North Atlantic Ocean) in 57.5 ka BP maximal relative to minimal because the ice sheet volume difference in between maximal and minimal scenario is lower during 57.5 ka than in 45 ka BP (Fig. 2.3). The presence of the LIS amplifies the atmospheric stationary waves, leading to an enhanced and northwardshifted jet stream, with stronger and southward-shifted wind barbs at the ocean surface. The simulated 57.5 ka BP (45 ka BP)-maximal global mean precipitation is ~0.36 mm/month (~3.81 mm/month) higher than the 57.5 ka BP (45 ka BP)-maximal, repectively.

The tropical rain belt experiences more precipitation in winter than summer and annual over the southern parts of tropics specially over the Southeast Asian countries and Indian Ocean than the both mid & higher latitude hemisphere, indicating a southward displacement of the ITCZ. Wetter conditions over West Africa and Southeast Asia are a sign of an increased summer monsoons. Dry conditions appear over the North Atlantic Ocean and Northern continents as a consequence of a colder and drier atmosphere during MIS 3.

The simulated global mean sea ice concentration in 57.5 ka BP (45 ka BP)-maximal is ~1.60% (~3.10%) thicker than the 57.5 ka BP (45 ka BP)-minimal, respectively. During MIS 3 (in both maximal and minimal scenario) sea ice is notably thicker and greater in extent in both hemispheres and seasons. Arctic sea ice is more thicker and extends further equatorward in the Pacific during winter. The Nordic Seas are partly ice-covered in boreal summer; in winter, sea ice extent is greater but includes an opening in the south due to the intrusion of warm Atlantic water. In the Southern Hemisphere, Antarctic sea ice is thicker (mainly in the western Indian Ocean sector) and extends further north. The simulated global mean SST at 57.5 ka BP (45 ka BP)-maximal is ~0.36 ^{0}C (~1.36 ^{0}C) cooler than the 57.5 ka BP (45 ka BP)-maximal, repectively. Simulated seasonal mean of SST at 45 ka BP-maximal is colder than that at 45 ka BP-minimal with a pattern of modest cooling in the tropics and enhanced cooling at high latitudes, but warmer in case of 57.5 ka BP-maximal than 57.5 ka BP-minimal due to the geographical distribution of the warming reflect the change in surface air temperature, as shown in Fig. 3.1. The North Atlantic subpolar and North Pacific region are simulated by warming due to enhanced northward ocean heat transport from equator by ocean circulation (AMOC) and in the North Pacific associated with the surface air temperature at 57.5 ka (maximal - minimal).

The ocean temperature response to variations in AMOC strength by performing a set of freshwater hosing/extraction experiments under MIS 3 (57.5 ka & 45 ka BP) glacial boundary conditions using the comprehensive coupled climate model AWI-ESM-2.1. The upper cell of the AMOC is deepened and intensified under the influence of competing factors from both hemispheres: the cutoff of freshwater input due to the closed Bering Strait and the strengthened surface wind in the NH subpolar region both tend to invigorate the

AMOC. In the Southern Ocean, expansion of Antarctic sea ice stimulates AABW production by enhanced salt rejection and deep water production. The results are supported by marine proxy records indicating an AMOC comparable to the present day during the last glacial (except during Heinrich stadials).

This thesis is limited to the study of MIS 3 maximal climate relative to the minimal ice sheet scneario, the challenge of understanding the large differences between maximal and minimal MIS 3 climate as inferred from proxy data remains. For future studies, the multi-stability of the climate-ice sheet system should be further investigated with a complex Earth system model. In addition, only the dynamic Northern Hemisphere ice sheets are included in the current study, a dynamic Antarctica should also be included as a next step.

Acronyms

AABW: Antarctic Bottom Water

AMOC: Atlantic meridional overturning circulation

AWI-CM: AWI Climate Model,

AWI-ESM: Alfred Wegener Institute– Earth System Model

CDO: Climate Data Operator

DJF: December–January–February

ECHAM: European Centre Hamburg Model

ECMWF: European Centre Medium-Range Weather Forecasts

FESOM: Finite-Element Sea Ice–Ocean Model

GHGs: Green-House Gases

GIA: Glacial isostatic adjustment

ITCZ: Intertropical Convergence Zone

JJA: June–July–August

ka BP: Thousand Years Before Present

LGM: Last Glacial Maximum

LIS: Laurentide Ice Sheet

MAM: March–April–May

MIS 3: Marine Isotope Stage 3

MPI-M: Max Planck Institute for Meteorology

NADW: North Atlantic Deep Water

NH: Northern Hemisphere

PI: Pre-Industrial

SH: Southern Hemisphere

SON: September–October–November

SST: Sea Surface Temperature

T_{2m}: 2m Air Temperature

Bibliography

Abe-Ouchi, A., Segawa, T., and Saito, F. (2007), Climatic Conditions for modelling the Northern Hemisphere ice sheets throughout the ice age cycle. *Climate of Past*, 3(3), 423–438.

Adkins, J. F., McIntyre, K., and Schrag, D. P. (2002), The Salinity, Temperature, and δ18O of the Glacial Deep Ocean. *Science*, 298(5599), 1769– 1773.

Andrews JT. (2000), Dating glacial events and correlation to global climate change. In: Noller JS.,Sowers JM., Lettis WR. (eds) (2000) Quaternary geochronology, methods and applications. *American Geophysical Union, AGU Reference Shelf*, 4, 447–455.

Barron, E. and Pollard, D. (2002), High-Resolution Climate Simulations of Oxygen Isotope Stage 3 in Europe. *Quaternary Research*, 58(3), 296– 309.

Batchelor, C. L. et al. The configuration of Northern Hemisphere ice sheets through the Quaternary. *Nature communications* 10, 1–10 (2019).

Berger, A. L. (1978), Long-term variations of caloric insolation resulting from the earth's orbital elements. *Quaternary Research*, 9(2), 139–167.

Bleck, R., Rooth, C., Hu, D., and Smith, L. T. (1992), Salinity-driven Thermocline Transients in a Wind- and Thermohaline-forced Isopycnic Coordinate Model of the North Atlantic. *Journal of Physical Oceanography*, 22(12), 1486–1505.

Böhm, E., Lippold, J., Gutjahr, M., Frank, M., Blaser, P., Antz, B., Fohlmeister, J., Frank, N., Andersen, M. B., and Deininger, M.: Strong and deep Atlantic meridional overturning circulation during the last glacial cycle, *Nature*, 517, 73–76.

Bond, G., Showers, W., Cheseby, M., Lotti, R., Almasi, P., deMenocal, P., Priore, P., Cullen, H., Hajdas, I., and Bonani, G. (1997), A Pervasive Millennial-Scale Cycle in North Atlantic Holocene and Glacial Climates. *Science*, 278(5341), 1257–1266.

Braconnot P, Otto-Bliesner B, Harrison S et al. (2007) Results of PMIP2 coupled simulations of the mid-Holocene and last glacial maximum–part 1: Experiments and large-scale features. *Climate of the Past*, 3(2), 261–277.

Braconnot, P., S. P. Harrison, M. Kageyama, P. J. Bartlein, V. Masson-Delmotte, A. Abe-Ouchi, B. L. Otto-Bliesner, and Y. Zhao (2012), Evaluation of climate models using palaeoclimatic data. *Nat. Clim. Change*, 2(6), 417–424.

Brandefelt, J. and Otto-Bliesner, B. L (2009), Equilibration and variability in a Last Glacial Maximum climate simulation with CCSM3. *Geophysical Reaserch Letters*, 36(19), L19712.

Brandefelt, J., Kjellström, E., Näslund, J.-O., Strandberg, G., Voelker, A. H. L., and Wohlfarth, B. (2011), A coupled climate model simulation of Marine Isotope Stage 3 stadial climate. *Climate of Past*, 7(2), 649–670.

Broecker, W. S. (1994), Massive iceberg discharges as triggers for global climate change. *Nature*, 372(6505), 421–424.

Broecker, W. S. (1990). Salinity history of the northern Atlantic during the last deglaciation. *Paleoceanography*, 5(4), 459–467.

Broecker, W. S. (2000). Was a change in thermohaline circulation responsible for the little ice age? *Proceedings of the National Academy of Sciences*, 97(4), 1339–1342.

Broecker, W. S., Andree, M., Wolfli, W., Oeschger, H., Bonani, G., Kennett, J., & Peteet, D. (1988). The chronology of the last Deglaciation: Implications to the cause of the Younger Dryas event. *Paleoceanography*, 3(1), 1–19.

Broecker, W. S., Peteet, D. M., & Rind, D. (1985). Does the ocean atmosphere system have more than one stable mode of operation? *Nature*, 315(6014), 21–26.

Brown, N. and Galbraith, E. D. (2016): Hosed vs. unhosed: interruptions of the Atlantic Meridional Overturning Circulation in a global coupled model, with and without freshwater forcing, *Clim. Past*, 12, 1663–1679.

Bryan, F. (1986). High-latitude salinity effects and interhemispheric thermohaline circulations. *Nature*, 323(6086), 301–304.

Calov, R., Greve, R., (2005). A semi-analytical solution for the positive degree-day model with stochastic temperature variations. *J. Glaciol.* 51, 173–175.

Clark, P. U., Pisias, N. G., Stocker, T. F., & Weaver, A. J. (2002). The role of the thermohaline circulation in abrupt climate change. *Nature*, 415(6874), 863–869.

Crucifix M., Braconnot P., Harrison S. et al. (2005), Second phase of paleoclimate modelling intercomparison project. *Eos Transactions American Geophysical Union*, 86(28), 264–264.

Curry, W. B. and Oppo, D. W. (2005): Glacial water mass geometry and the distribution of δ 13C of 6CO2 in the western Atlantic Ocean, *Paleoceanography*, 20, PA1017.

Dalton, A. S. et al. (2019), Was the Laurentide Ice Sheet significantly reduced during marine isotope stage 3? *Geology*, 47(2), 111–114.

Danilov, S., Sidorenko, D. Wang, Q., and Jung, T. (2017), The Finite-volumE Sea ice– Ocean Model (FESOM2). *Geoscientific Model Development*, 10(2), 765-789.

Dansgaard, W. et al. (1993), Evidence for general instability of past climate from a 250-kyr ice-core record. *Nature*, 364(6434), 218–220.

Davis B, Brewer S, Stevenson A et al. (2003) The temperature of Europe during the Holocene reconstructed from pollen data. *Quaternary Science Reviews*, 22(15), 1701–1716.

Dokken, T. M., Nisancioglu, K. H., Li, C., Battisti, D. S., and Kissel, C. (2013), Dansgaard Oeschger cycles: Interactions between ocean and sea ice intrinsic to the Nordic seas. *Paleoceanography*, 28(3), 491– 502.

Egbert, G. D., Ray, R. D., and Bills, B. G. (2004), Numerical modeling of the global semidiurnal tide in the present day and in the last glacial maximum. *Journal Geophysical Research Ocean*, 109(3), C03003.

Ezat, M. M., Rasmussen, T. L., and Groeneveld, J.: Persistent intermediate water warming during cold stadials in the southeastern Nordic seas during the past 65 k.y., *Geology*, 42, 663– 666, 2014.

Ferrari, R., Jansen, M. F., Adkins, J. F., Burke, A., Stewart, A. L., and Thompson, A. F. (2014): Antarctic sea ice control on ocean circulation in present and glacial climates, P. Natl. *Acad. Sci. USA*, 111, 8753–8758.

Fisher, D., Reeh, N. & Langley, K. Objective reconstructions of the Late Wisconsinan Laurentide Ice Sheet and the significance of deformable beds. *Geographie Physique et Quaternaire* 39, 229–238 (1985).

Ganopolski, A. and Rahmstorf, S. (2001), Rapid changes of glacial climate simulated in a coupled climate model. *Nature*, 409(6817), 153– 158.

Gierz P., Werner M. and Lohmann G. (2017), Simulating climate and stable water isotopes during the Last Interglacial using a coupled climate-isotope model. *Journal of Advances in Modelling Earth Systems*, 9(5), 2027-2045.

Gierz, P., Lohmann, G., & Wei, W. (2015). Response of Atlantic overturning to future warming in a coupled atmosphere-ocean-ice sheet model: Response of AMOC in a coupled GCM-ISM. *Geophysical Research Letters*, 42, 6811–6818.

Gong, X., Knorr, G., Lohmann, G., and Zhang, X. (2013), Dependence of abrupt Atlantic meridional ocean circulation changes on climate background states. Geophysical Reaserch Letters, 40(14), 3698–3704.

Gowan, E.J., X. Zhang, S. Khosravi, A. Rovere, P. Stocchi, A. L. C. Hughes, R. Gyllencreutz, J. Mangerud, J. I. Svendsen, G. Lohmann, (2021). A new global ice sheet reconstruction for the past 80,000 years. *Nature communications*, 12, 1199.

Heinrich, H. (1988), Origin and consequences of cyclic ice rafting in the Northeast Atlantic Ocean during the past 130,000 years. *Quaternary Research*, 29(2), 14–152.

Henry, L. G., McManus, J. F., Curry, W. B., Roberts, N. L., Piotrowski, A. M., and Keigwin, L. D. (2016), North Atlantic ocean circulation and abrupt climate change during the last glaciation. *Science*, 353(6298), 470–474.

Haywood, A. M., et al. (2013), Large-scale features of Pliocene climate: Results from the Pliocene Model Intercomparison Project, *Clim. Past*, 9(1), 191–209.

Hays J. D., John Imbrie, N. J. Shackleton (1976), Variations in the Earth's Orbit: Pacemaker of the Ice Ages, Science, New Series, *American Association for the Advancement of Science*, 194, 4270, pp. 1121-1132.

Hu, A., Meehl, G. A., Otto-Bliesner, B. L., Waelbroeck, C., Han, W., Loutre, M.-F., Lambeck, K., Mitrovica, J. X., and Rosenbloom, N. (2010): Influence of Bering Strait flow and North Atlantic circulation on glacial sea-level changes, *Nat. Geosci.*, 3, 118–121.

Hu, A., Meehl, G. A., Han, W., Otto-Bliestner, B., AbeOuchi, A., and Rosenbloom, N. (2015): Effects of the Bering Strait closure on AMOC and global climate under different background climates, *Prog. Oceanogr.*, 132, 174–196.

Huber, C., Leuenberger, M., et al. (2006), Isotope calibrated Greenland temperature record over Marine Isotope Stage 3 and its relation to CH4. *Earth and Planetary Science Letters*, 243(3- 4), 504–519.

Hurrell JW. (1995), Decadal trends in The North Atlantic oscillation: Regional temperatures and precipitation. *Science*, 269(5224), 676–679.

Ingólfsson, Ó. & Landvik, J. Y., (2013), The Svalbard– Barents Sea ice-sheet – Historical, current and future perspectives. *Quaternary Science Review*, 64, 33–60.

Jansen, M. F. (2017): Glacial ocean circulation and stratification explained by reduced atmospheric temperature, P. Natl. *Acad. Sci. USA*, 114, 45–50.

Joussaume S. and Braconnot P. (1997), Sensitivity of paleoclimate simulation results to season definitions. *Journal of Geophysical Research: Atmospheres*, 102(D2), 1943–1956.

Jungclaus J., Fischer N., Haak H. et al. (2013), Characteristics of the ocean simulations in the Max Planck Institute Ocean Model (MPIOM) the ocean component of the MPI- earth system model. *Journal of Advances in Modeling Earth Systems*, 5(2), 422–446.

Klockmann, M., Mikolajewicz, U., and Marotzke, J. (2016): The effect of greenhouse gas concentrations and ice sheets on the glacial AMOC in a coupled climate model, *Clim. Past*, 12, 1829–1846.

Knorr, G., & Lohmann, G. (2007). Rapid transitions in the Atlantic thermohaline circulation triggered by global warming and meltwater during the last deglaciation. *Geochemistry, Geophysics, Geosystems*, 8, Q12006.

Knutti, R., R. Furrer, C. Tebaldi, J. Cermak, and G. A. Meehl (2010), Challenges in combining projections from multiple climate models, *J. Clim*., 23(10), 2739–2758.

Köhler P., Nehrbass-Ahles C., Schmitt J. et al. (2017), A 156 kyr smoothed history of the atmospheric greenhouse gases CO2, CH4, and N2O and their radiative forcing. *Earth System Science Data*, 9(1), 363–387.

Lohmann, G., Butzin, M., Eissner, N., Shi, X., and Stepanek, C. (2020). Abrupt climate and weather changes across time scales. *Paleoceanography and Paleoclimatology*, 35(9)e2019PA003782.

Lohmann, G., M. Pfeiffer, T. Laepple, G. Leduc, and J. H. Kim (2013a), A model–data comparison of the Holocene global sea surface temperature evolution, *Clim. Past*, 9(4), 1807–1839.

Lott F (1999) Alleviation of stationary biases in a GCM through a mountain drag parameterization scheme and a simple representation of mountain lift forces. *Monthly Weather Review* 127(5), 788–801.

Li, C., Battisti, D. S., and Bitz, C. M. (2010), Can North Atlantic Sea Ice Anomalies Account for Dansgaard– Oeschger Climate Signals? *Journal of Climate*, 23(20), 5457–5475.

Lu H., Yi S., Liu Z. et al. (2013), Variation of East Asian monsoon precipitation during the past 21 ky and potential CO2 forcing. *Geology*, 41(9), 1023–1026.

Lynch-Stieglitz, J. (2017): The Atlantic Meridional Overturning Circulation and Abrupt Climate Change, *Annu. Rev. Mar. Sci.*, 9, 83–104.

Manabe, S., & Stouffer, R. J. (1995). Simulation of abrupt climate change induced by freshwater input to the North Atlantic Ocean. *Nature*, 378(6553), 165–167.

Martinson, D., Pisias, N., Hays, J., Imbrie, J., Moore, T., & Shackleton, N. (1987). Age Dating and the Orbital Theory of the Ice Ages: Development of a High-Resolution 0 to 300,000-Year Chronostratigraphy. *Quaternary Research, 27*(1), 1-29.

Milankovic, M., Berger, A., and Milankovic, V. (1995). Milutin Milankovic 1879-1958: From His Autobiography with Comments by His Son, Vasko and a Preface by André Berger. *European Geophysical Society*.

Montoya, M. and Levermann, A. (2008): Surface wind-stress threshold for glacial Atlantic overturning, *Geophys. Res. Lett*., 35, L03608.

Muglia, J. and Schmittner, A. (2015): Glacial Atlantic overturning increased by wind stress in climate models. *Geophys. Res. Lett.*, 42, 9862–9868.

Munk, W. H. (1966): Abyssal recipes, Deep-Sea Res. *Oceanogr. Abstr.*, 13, 707–730.

Naslund, J.-O., Wohlfarth, B., et al. (2008), Fennoscandian paleo-environment and ice sheet dynamics during Marine Isotope Stage 3.

O'Mahony, M. (1986). Sensory evaluation of food: statistical methods and procedures, volume 16. *CRC Press.*

Oka, A., Hasumi, H., and Abe-Ouchi, A. (2012): The thermal threshold of the Atlantic meridional overturning circulation and its control by wind stress forcing during glacial climate, *Geophys. Res. Lett.*, 39, L09709.

Otto-Bliesner BL, Braconnot P, Harrison SP et al. (2017) The PMIP4 contribution to CMIP6-Part 2: Two interglacials, scientific objective and experimental design for Holocene and Last Interglacial Simulations. *Geoscientific Model Development*, 10(11), 3979–4003.

Peltier, W. R., Argus, D. F., and Drummond, R. (2015), Space geodesy constrains ice age terminal deglaciation: The global ICE-6G_C (VM5a) model. *JGR Solid Earth*, 120(1), 450– 487.

Peltier, W. R. and Vettoretti, G. (2014): Dansgaard-Oeschger oscillations predicted in a comprehensive model of glacial climate: A "kicked" salt oscillator in the Atlantic, *Geophys. Res. Lett.*, 41, 7306–7313.

Pfeiffer, M., and G. Lohmann (2016), Greenland Ice Sheet influence on Last Interglacial climate: Global sensitivity studies performed with an atmosphere–ocean general circulation model, *Clim. Past*, 12(6), 1313–1338.

Rackow T., Goessling HF., Jung T. et al. (2018), Towards multiresolution global climate modeling with ECHAM6-FESOM. Part II: Climate variability. *Climate Dynamics*, 50(7–8), 2369–2394.

Rahmstorf, S. (2002). Ocean circulation and climate during the past 120,000 years. *Nature*, 419, 207–214.

Raynaud D., Barnola J., Chappellaz J. et al. (2000), The ice record of greenhouse gases: A view in the context of future changes. *Quaternary Science Reviews*, 19(1–5), 9–17.

Reeh, N. A plasticity theory approach to the steady-state shape of a three-dimensional ice sheet. *Journal of Glaciology*, 28, 431–455 (1982).

Reeh, N., (1989). Parameterization of melt rate and surface temperature on the Greenland ice sheet. *Polarforschung* 59, 113–128.

Roeckner E., Dümenil L., Kirk E. et al. (1989), The Hamburg version of the ECMWF model (ECHAM). *Technical Report*, 13, 7–1.

Schmittner, A., Green, J. A. M., and Wilmes, S.-B. (2015): Glacial ocean overturning intensified by tidal mixing in a global circulation model, *Geophys. Res. Lett.*, 42, 4014–4022.

Scholz P., Kieke D., Lohmann G. et al. (2014), Evaluation of Labrador Sea Water formation in a global Finite-Element Sea-Ice Shi et al. 1015 Ocean Model setup, based on a comparison with observational data. *Journal of Geophysical Research: Oceans,* 119(3), 1644–1667.

Scholz P., Lohmann G., Wang Q. et al. (2013), Evaluation of a Finite-Element Sea-Ice Ocean Model (FESOM) set-up to study the interannual to decadal variability in the deep-water formation rates. *Ocean Dynamics,* 63(4), 347–370.

Schulzweida, U., Kornblueh, L., and Quast, R. (2006). Cdo user's guide. Climate data operators, Version, 1(6), 205–209.

Sherriff-Tadano, S., Abe-Ouchi, A., Yoshimori, M., Oka, A., and Chan, W.-L. (2018): Influence of glacial ice sheets on the Atlantic meridional overturning circulation through surface wind change, *Clim. Dynam.*, 50, 2881–2903.

Shi X and Lohmann G (2016) Simulated response of the midHolocene Atlantic meridional overturning circulation in ECHAM6-FESOM/MPIOM. *Journal of Geophysical Research Oceans,* 121(8), 6444–6469.

Shi, X., Lohmann, G., Sidorenko, D., and Yang, H. (2020). Early-holocene simulations using different forcings and resolutions in awi-esm. The Holocene, page 0959683620908634.

Shin, S.-I., Liu, Z., Otto-Bliesner, B. L., Kutzbach, J. E., and Vavrus, S. J. (2003): Southern Ocean sea-ice control of the glacial North Atlantic thermohaline circulation, *Geophys. Res. Lett.*, 30, 1096.

Sidorenko, D., Goessling, H. F., Koldunov, N., Scholz, P., Jung. T. et al. (2019), Evaluation of FESOM2.0 Coupled to ECHAM6.3: Preindustrial and HighResMIP Simulations. *Journal of Advances in Modeling Earth Systems,* 11(11), 3794-3815.

Sidorenko D., Rackow T., Jung T. et al. (2015), Towards multi-resolution global climate modeling with ECHAM6–FESOM. Part I: Model formulation and mean climate. *Climate Dynamics*, 44(3–4), 757–780.

Stevens B., Giorgetta M., Esch M. et al. (2013), Atmospheric component of the MPI-M earth system model: ECHAM6. *Journal of Advances in Modeling Earth Systems*, 5(2), 146– 172.

Stocker, T. F. (1998), The seesaw effect. *Science*, 282(5386), 61–62.

Sundqvist H, Berge E and Kristjánsson JE (1989) Condensation and cloud parameterization studies with a mesoscale numerical weather prediction model. *Monthly Weather Review,* 117(8), 1641–1657.

Timm, O., Timmermann, A., Abe-Ouchi, A., Saito, F., and Segawa, T. (2008). On the definition of seasons in paleoclimate simulations with orbital forcing. *Paleoceanography*, 23(2).

Timmermann R., Danilov S., Schröter J. et al. (2009), Ocean circulation and sea ice distribution in a finite element global sea ice-ocean model. *Ocean Modelling,* 27(3-4), 114–129.

Van Meerbeeck, C. J., Renssen, H., and Roche, D. M. (2009), How did Marine Isotope Stage 3 and Last Glacial Maximum climates differ? – Perspectives from equilibrium simulations. *Climate of Past*, 5(1), 33–51.

Wang Q., Danilov S., Sidorenko D. et al. (2014), The Finite Element Sea Ice-Ocean Model (FESOM): Formulation of an unstructured-mesh ocean general circulation model. *Geoscientific Model Development*, 7(2), 663–693.

Weber S. (2001), The impact of orbital forcing on the climate of an intermediate- complexity coupled model. *Global and Planetary Change*, 30(1), 7–12.

Wekerle C. (2013), Dynamics of the Canadian arctic archipelago throughflow: A numerical study with a finite element sea ice and ocean model. PhD Thesis, Alfred-Wegener-Institut, Universitaet Bremen.

Zhang X., Lohmann G., Knorr G. et al. (2014a). Abrupt glacial climate shifts controlled by ice sheet changes. *Nature*, 512(7514), 290–294.

Zhang, X., Prange, M., Merkel, U., and Schulz, M. (2014b): Instability of the Atlantic overturning circulation during Marine Isotope Stage 3, *Geophys. Res. Lett.*, 41, 4285–4293.

Zhang Y, Renssen H, Seppä H et al. (2018) Holocene temperature trends in the extratropical northern hemisphere based on inter-model comparisons. *Journal of Quaternary Science*, 33(4), 464–476.

Appendix A

A.1 Atmospheric Surface Temperature: MIS 3 (maximal scenario) - PI

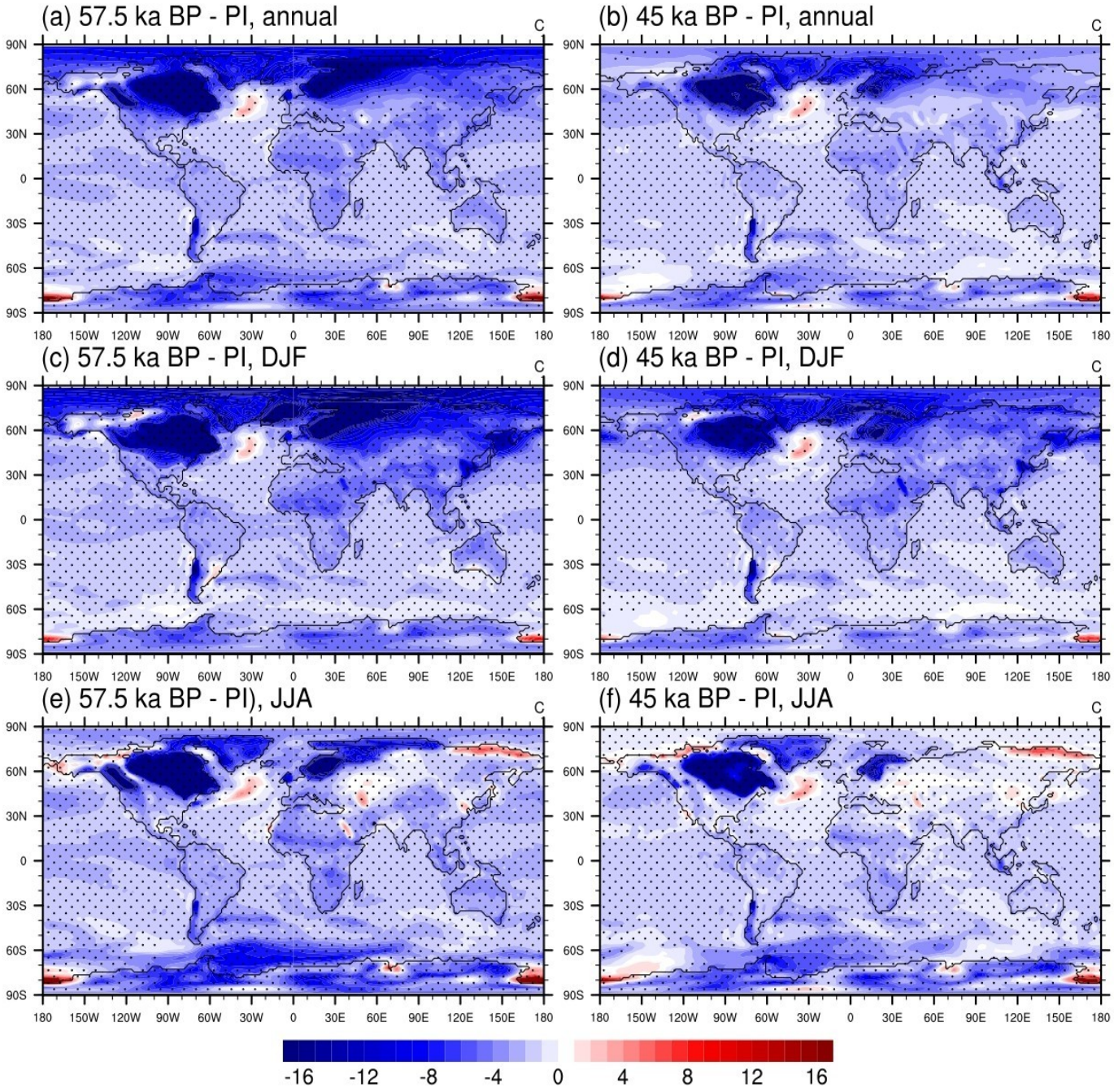

Figure A.1. Simulated 2m surface temperature anomalies of MIS 3 (maximal) relative to their corresponding PI with their respective land sea mask (coastline) for annual mean (a, b) and seasonal mean: winter - DJF (c, d) and summer - JJA (e, f). The marked area has a significance level of above 95% based on Student's t-test. Units are ^{0}C.

A.2 Atmospheric Surface Temperature: MIS 3 (minimal scenario) – PI

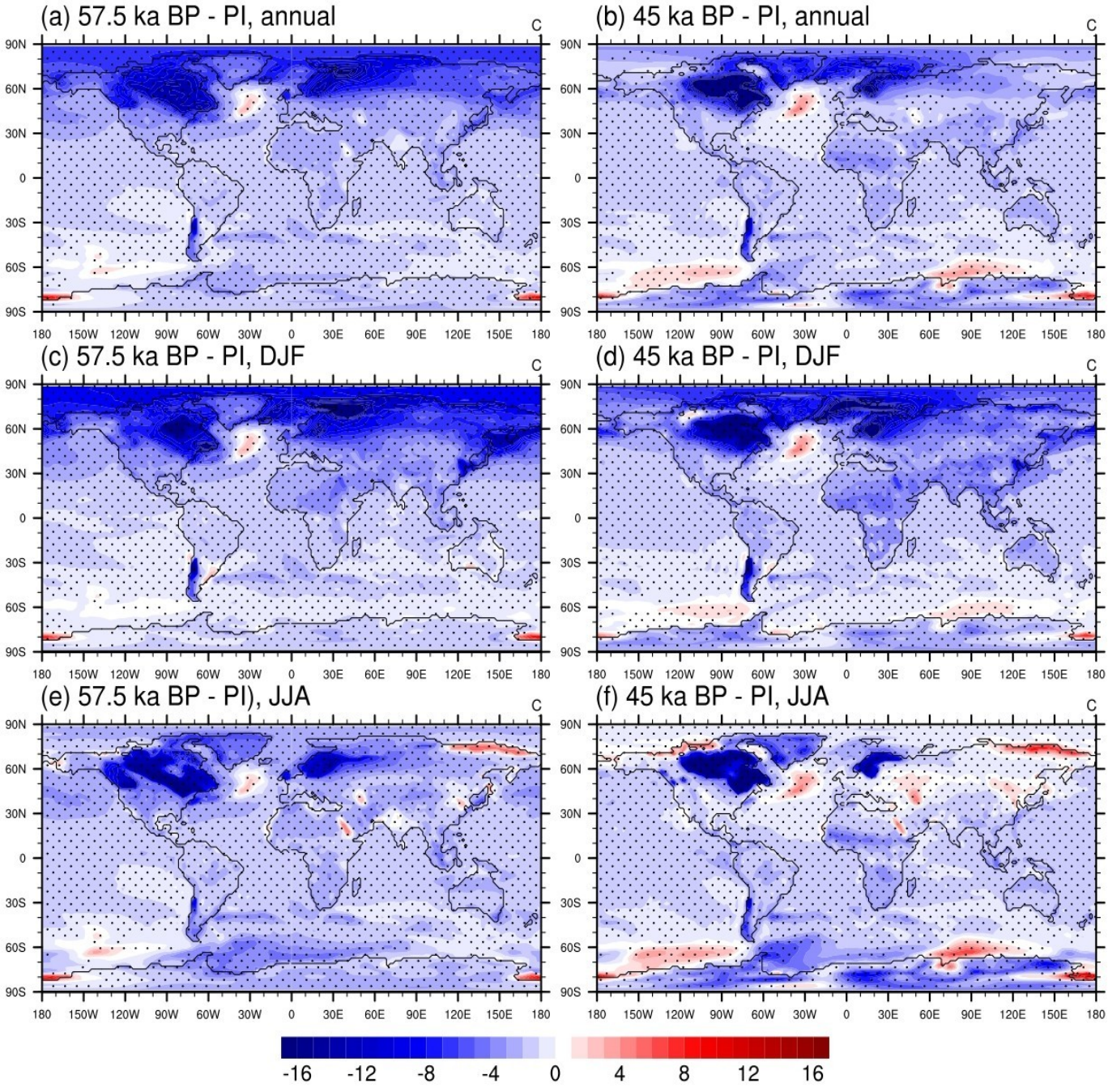

Figure A.2. Simulated 2m surface temperature anomalies of MIS 3 (minimal) relative to their corresponding PI with their respective land sea mask (coastline) for annual mean (a, b) and seasonal mean: winter - DJF (c, d) and summer - JJA (e, f). The marked area has a significance level of above 95% based on Student's t-test. Units are ^{0}C.

A.3 Geopotential Height and Wind Circulation: MIS 3 (maximal) - PI

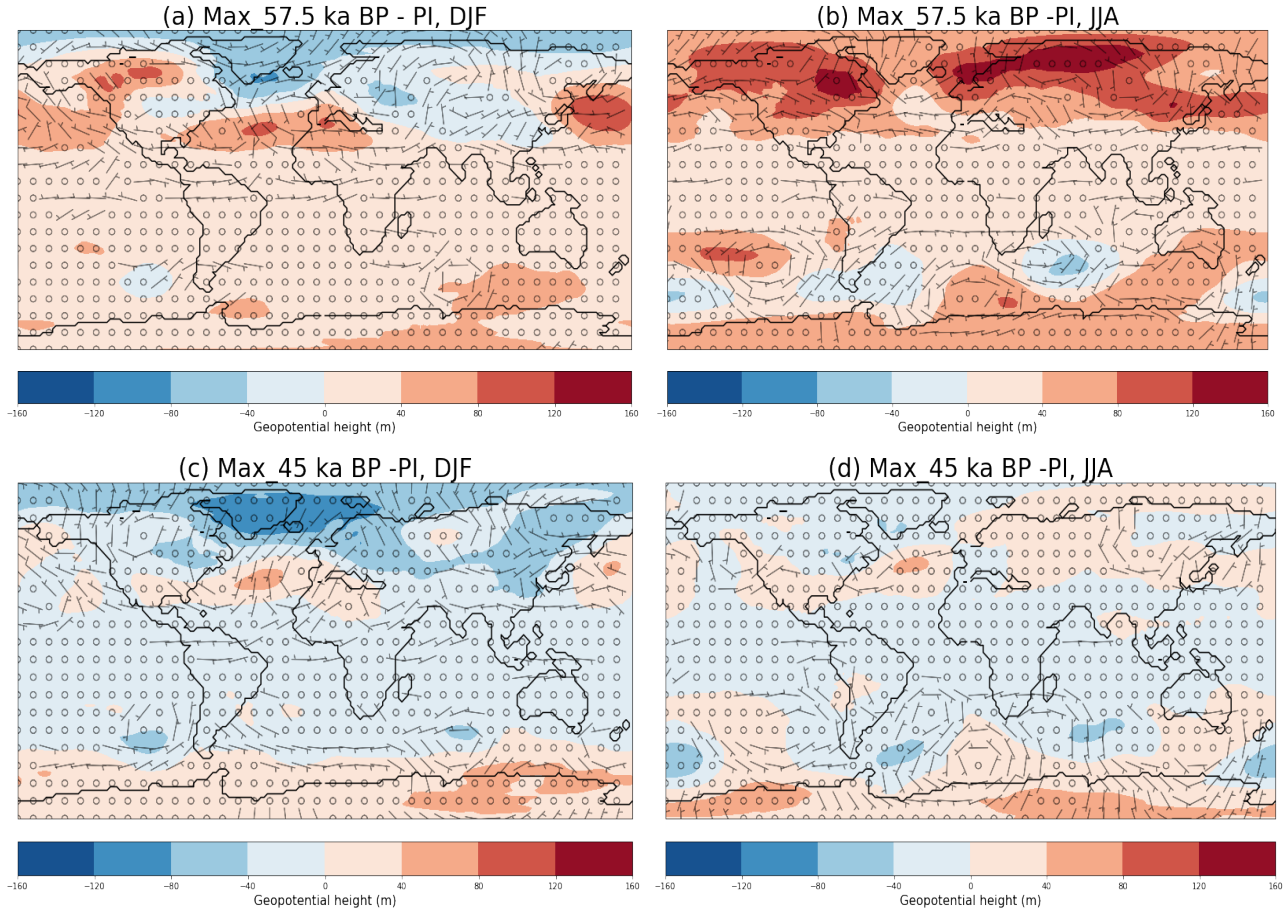

Figure A.3. Simulated 500 hpa geopotential height anomalies (m), Land – sea mask (coastline) and wind barb anomalies (kt) of MIS 3 (maximal) relative to PI for seasonal mean; (a, c) winter – DJF and (b, d) summer - JJA.

A.4 Geopotential Height and Wind Circulation: MIS 3 (minimal) - PI

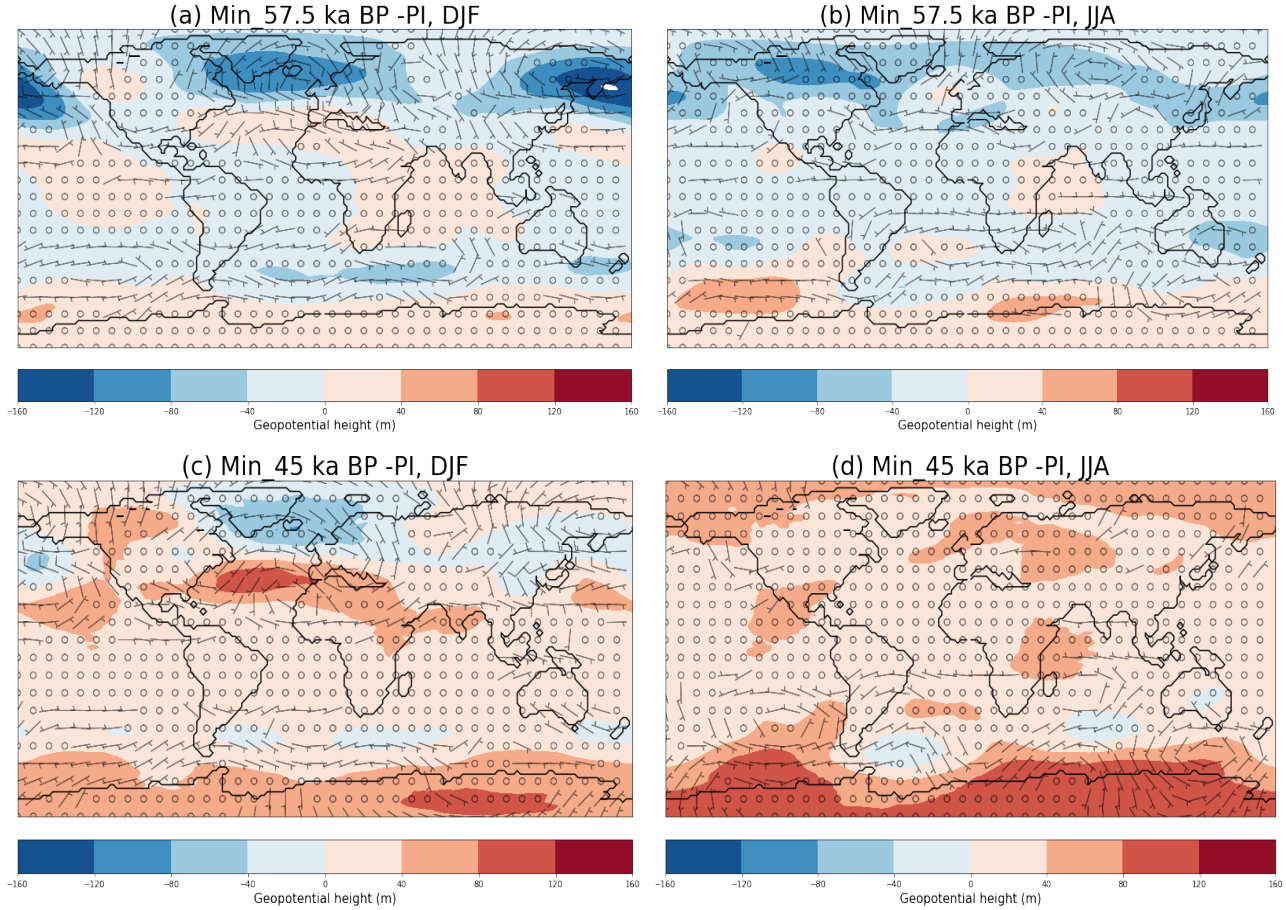

Figure A.4. Simulated 500 hpa geopotential height anomalies (m), Land – sea mask (coastline) and wind barb anomalies (kt) of MIS 3 (minimal) relative to PI for seasonal mean; (a, c) winter – DJF and (b, d) summer - JJA.

A.5 Geopotential Height and Wind Circulation: maximal

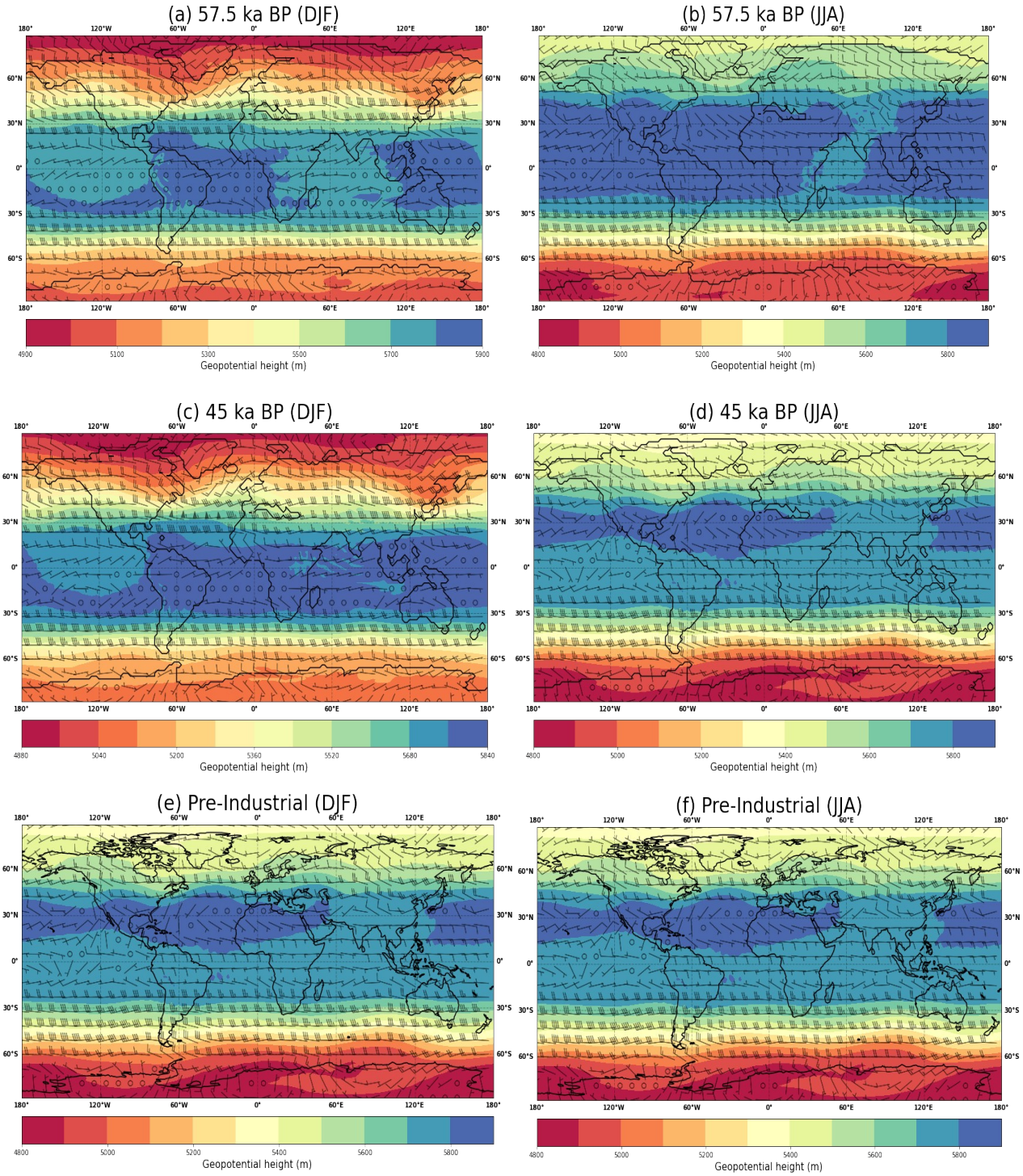

Figure A.5. Simulated 500 hpa geopotential height (m), Land – sea mask (coastline) and wind barb (kt) of MIS 3 (maximal) and PI for seasonal mean; (a, c, e) winter – DJF and (b, d, f) summer – JJA.

A.6 Geopotential Height and Wind Circulation: minimal

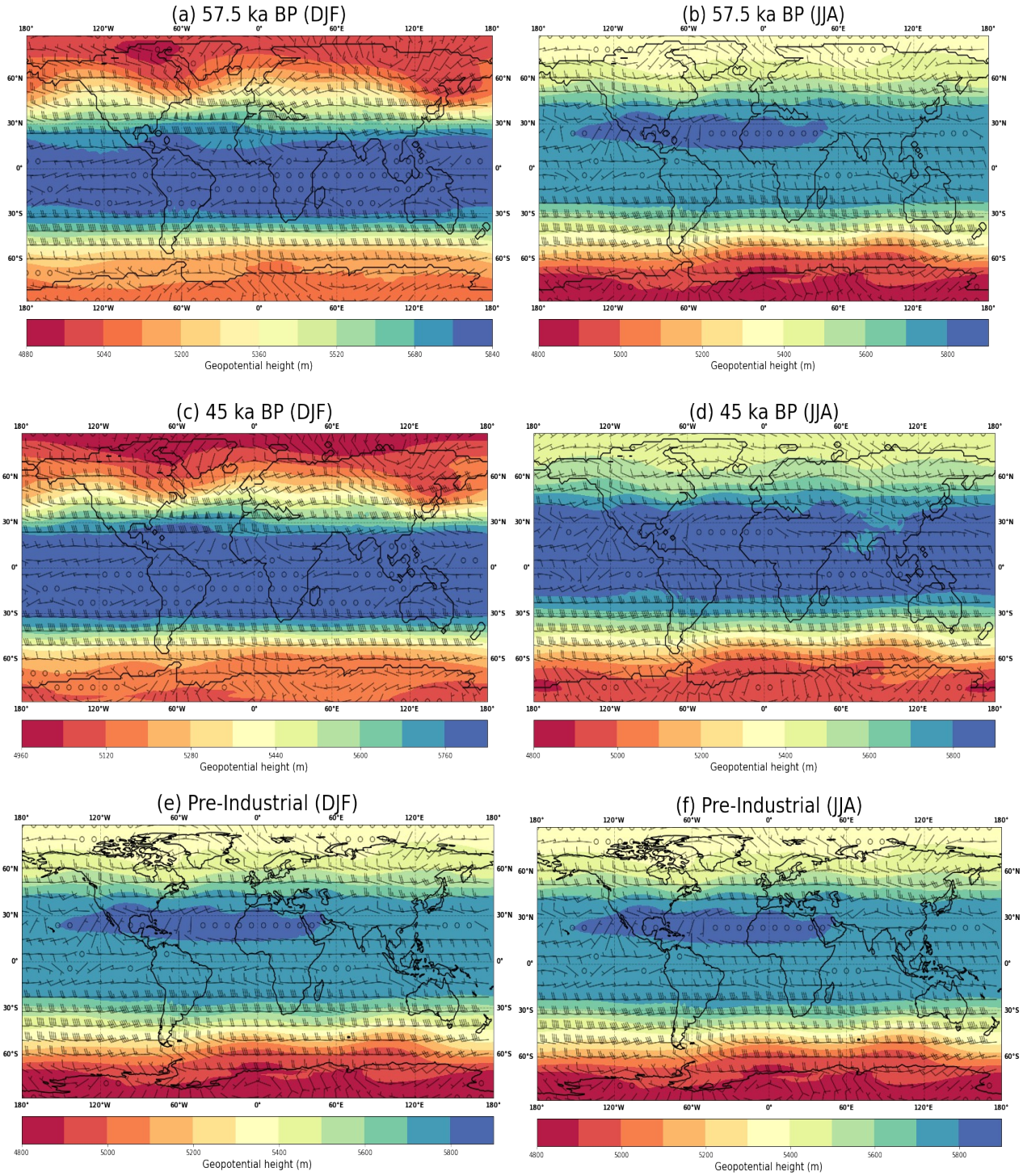

Figure A.6. Simulated 500 hpa geopotential height (m), Land – sea mask (coastline) and wind barb (kt) of MIS 3 (minimal) and PI for seasonal mean; (a, c, e) winter – DJF and (b, d, f) summer – JJA.

A.7 Total Precipitation: MIS 3 (maximal) - PI

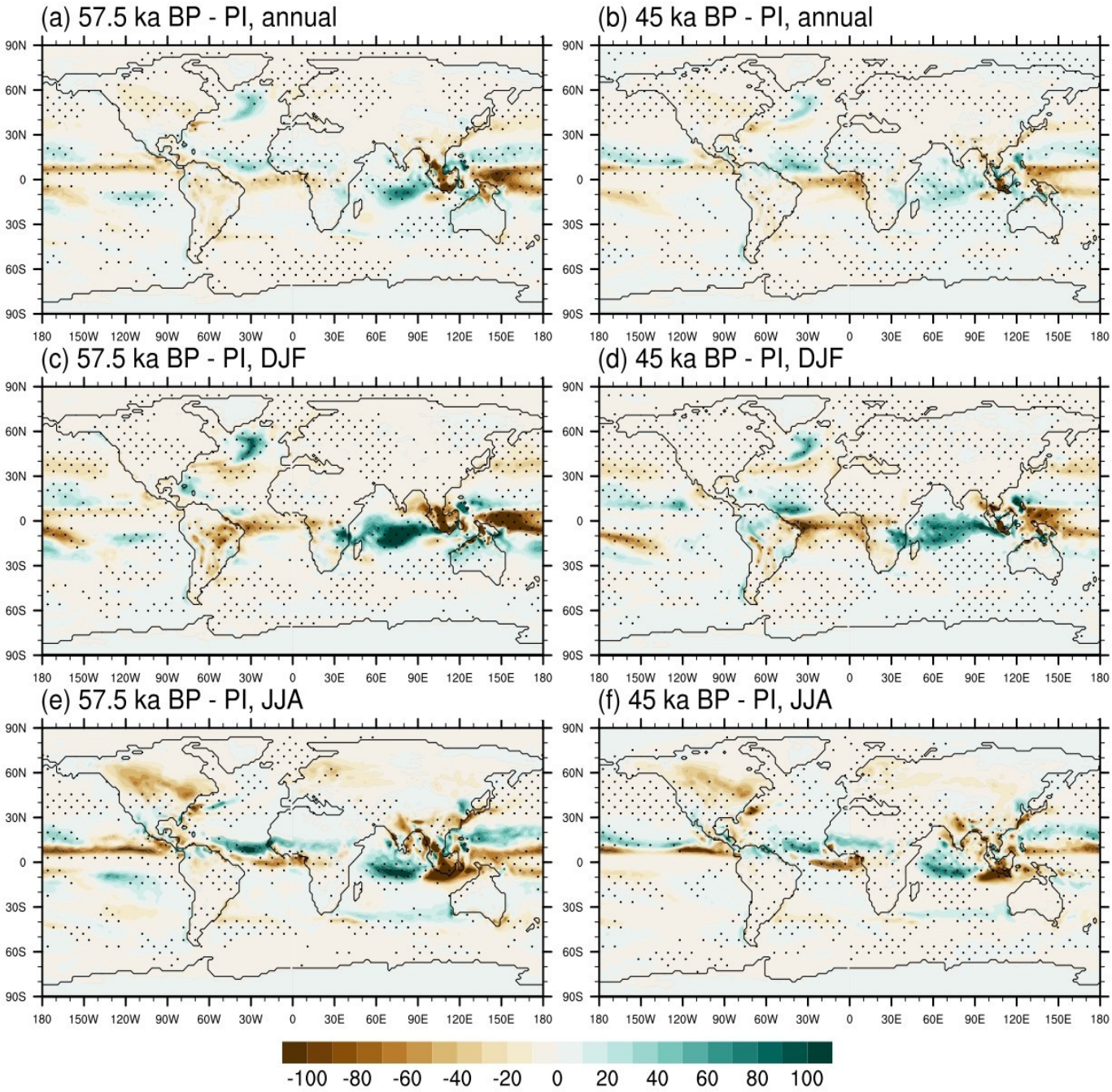

Figure A.7. Simulated total precipitation anomalies of MIS 3 (maximal) relative to their corresponding PI with their respective land sea mask (coastline) for annual mean (a, b) and seasonal mean: winter - DJF (c, d) and summer - JJA (e, f). The marked area has a significance level of above 95% based on Student's t-test. Units are mm/month.

A.8 Total Precipitation: MIS 3 (minimal) - PI

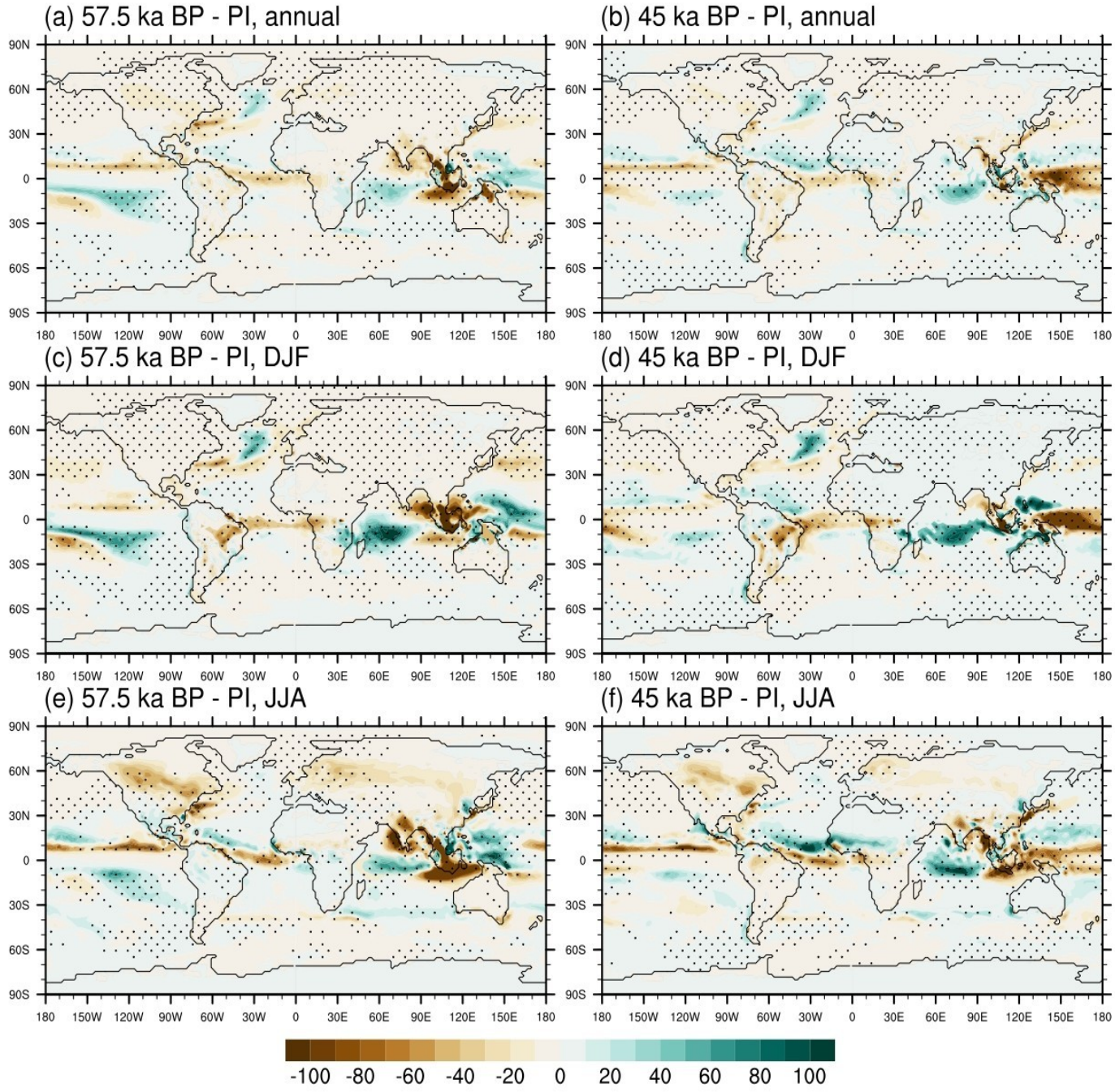

Figure A.8. Simulated total precipitation anomalies of MIS 3 (minimal) relative to their corresponding PI with their respective land sea mask (coastline) for annual mean (a, b) and seasonal mean: winter - DJF (c, d) and summer - JJA (e, f). The marked area has a significance level of above 95% based on Student's t-test. Units are mm/month.

A.9 Sea Surface Temperature: MIS 3 (maximal) - PI

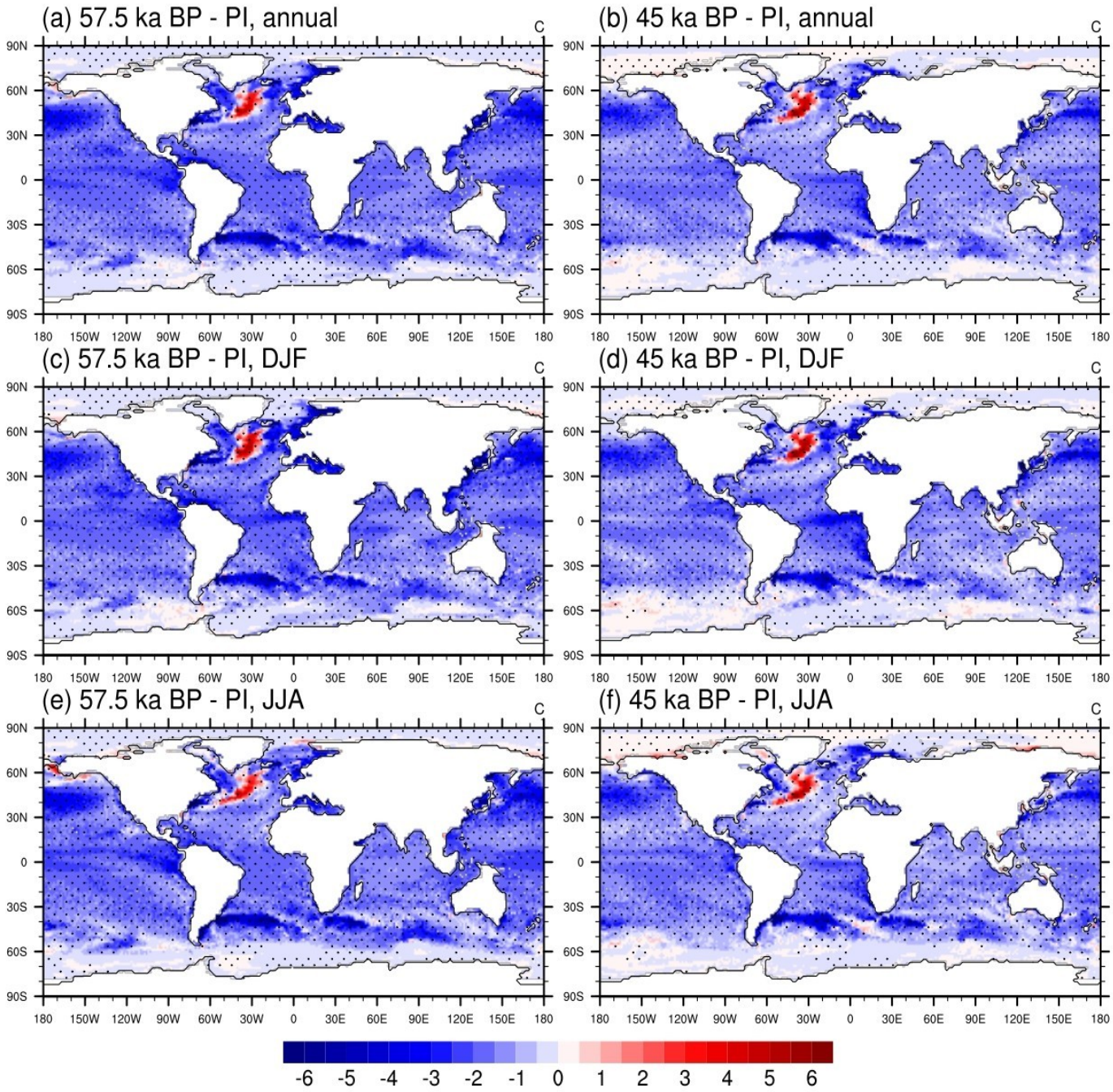

Figure A.9. Simulated sea surface temperature anomalies of MIS 3 (maximal) relative to their corresponding PI with their respective land sea mask (grey shading) for annual mean (a, b) and seasonal mean: winter - DJF (c, d) and summer - JJA (e, f). The marked area has a significance level of above 95% based on Student's t-test. Units are ^{0}C.

A.10 Sea Surface Temperature: MIS 3 (minimal) - PI

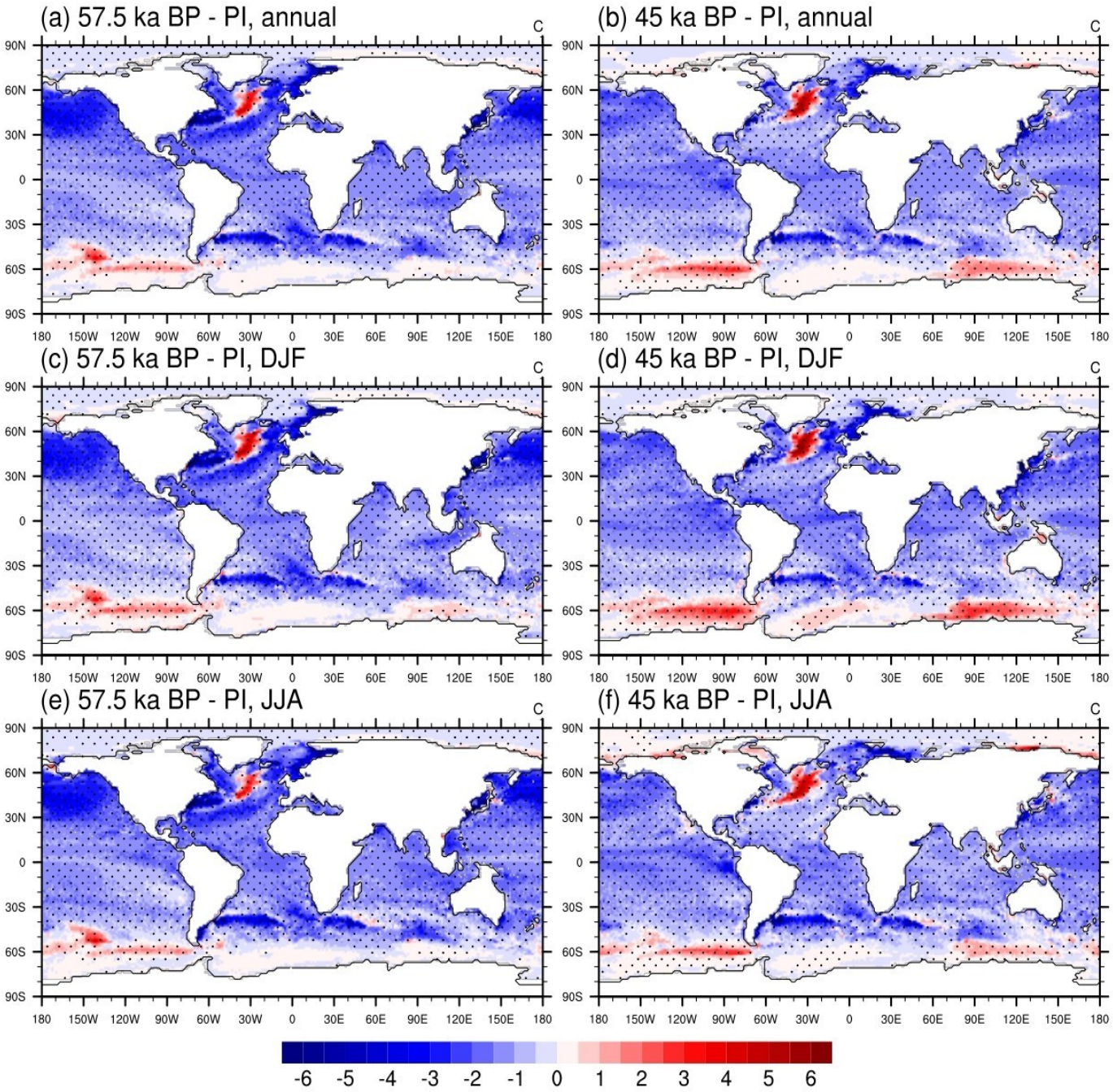

Figure A.10. Simulated sea surface temperature anomalies of MIS 3 (minimal) relative to their corresponding PI with their respective land sea mask (grey shading) for annual mean (a, b) and seasonal mean: winter - DJF (c, d) and summer - JJA (e, f). The marked area has a significance level of above 95% based on Student's t-test. Units are ^{0}C.